Li, Yulin; Yan, Haixian; Wang, Shiqi; Luo, Xuliang; Kurpaska, Łukasz; Fang, Feng; Jiang, Jianqing; Kim, Hyoung Seop; Huo, Wenyi

Toward predictable phase structures in high-entropy oxides : A strategy for screening multicomponent compositions

Published in:
Materials and Design

DOI:
10.1016/j.matdes.2024.113497

Published: 01/12/2024

Document Version
Publisher's PDF, also known as Version of record

Please cite the original version:
Li, Y., Yan, H., Wang, S., Luo, X., Kurpaska, Ł., Fang, F., Jiang, J., Kim, H. S., & Huo, W. (2024). Toward predictable phase structures in high-entropy oxides : A strategy for screening multicomponent compositions. *Materials and Design*, *248*, Article 113497. https://doi.org/10.1016/j.matdes.2024.113497

Materials & Design 248 (2024) 113497

Contents lists available at ScienceDirect

Materials & Design

journal homepage: www.elsevier.com/locate/matdes

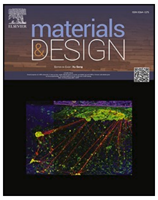

Toward predictable phase structures in high-entropy oxides: A strategy for screening multicomponent compositions

Yulin Li [a,1], Haixian Yan [c,1], Shiqi Wang [d], Xuliang Luo [e], Łukasz Kurpaska [a], Feng Fang [c,*], Jianqing Jiang [b,c], Hyoung Seop Kim [f,g,h], Wenyi Huo [a,b,*]

[a] NOMATEN Centre of Excellence, National Centre for Nuclear Research, Otwock 05-400, Poland
[b] College of Mechanical and Electrical Engineering, Nanjing Forestry University, Nanjing 210037, China
[c] Jiangsu Key Laboratory of Advanced Metallic Materials, Southeast University, Nanjing 211189, China
[d] Department of Chemistry, University of Helsinki, P.O. Box 55, Helsinki, FI 00014, Finland
[e] Department of Applied Physics, Aalto University, P.O. Box 11000, Aalto, FI 00076, Espoo, Finland
[f] Department of Materials Science and Engineering, Pohang University of Science & Technology (POSTECH), Pohang 37673, South Korea
[g] Advanced Institute for Materials Research (WPI-AIMR), Tohoku University, Sendai 980-8577, Japan
[h] Institute for Convergence Research and Education in Advanced Technology, Yonsei University, Seoul 03722, South Korea

ARTICLE INFO

Keywords:
High-entropy ceramics
High-entropy oxides
Phase selection engineering
Phase stability
Composition design

ABSTRACT

The recent surge in interest in high-entropy oxides (HEOs) as a novel class of ceramic materials can be attributed to the remarkable performance enhancements caused by both the complexity of their chemical composition and the simplicity of their structure. The extensive range of components presents challenges to the implementation of HEOs, rendering it difficult to predict the phase structure prior to the final synthesis. Herein, semi-empirical methods based on various parameters, including ΔX, VEC, ΔS_{mix}, ΔH_{mix} and δ, were utilized to determine the phase stability of rock salt, spinel, perovskite and fluorite structures. The combination of δ with ΔX, VEC, ΔS_{mix}, and ΔH_{mix}, in graphical form, is an effective indicator for determining the phase stability of rock salt, perovskite and fluorite structures. The spinel structure is stabilized outside the range of the other three structures. The phase formation rules were further verified with two newly designed and prepared HEOs via X-ray diffraction and high-resolution transmission electron microscopy. The HEOs show potential for functional applications, e.g., methyl orange degradation.

1. Introduction

Phase is a crucial structural parameter, alongside composition, morphology, architecture, facet, size, and dimensionality, that plays a fundamental role in determining the properties and functionalities of ceramics, e.g., oxides [1]. In particular, specific phases in oxides may endow oxides with interesting properties and novel applications [2]. Great progress has been made in the phase engineering of conventional ceramics, including phase selection, synthesis of ceramics with specific phases and unconventional phase transformation of ceramics [3,4].

The high-entropy effect was initially discovered by Cantor et al. [5] and Yeh et al. [6–8]. This effect can be defined as the phenomenon whereby the free energy of the solid solution phase can be reduced by increasing the mixing entropy, thus promoting the formation of the solid solution phase in high-entropy alloys (HEAs) [7,8]. This concept was subsequently broadened to include more materials, such as oxides [9], borides [10], nitrides [11], and phosphides [12]. High-entropy oxides (HEOs) are a class of oxide ceramic systems that use the phase stabilization effect of high configurational entropy to obtain a simple phase structure [13]. The initial HEO, comprising five elements, i.e., Co, Cu, Mg, Ni and Zn, exhibited a single rock salt phase and was first reported by Rost et al. [9]. Analogous to HEAs, the constituent elements of HEOs are in equimolar or near-equimolar ratios.

HEOs are divided into transition-metal-based HEOs (TM-HEOs) [9,14], rare-earth-based HEOs (RE-HEOs) [15,16] and mixed HEOs (TM-RE-HEOs) [17] according to their different components. Moreover, the combination of various elements in HEOs allows the formation of a variety of main crystalline phases, including rock salt, spinel, perovskite

---

* Corresponding authors.
E-mail addresses: fangfeng@seu.edu.cn (F. Fang), wenyi.huo@ncbj.gov.pl (W. Huo).

[1] These authors contributed equally to this paper.

https://doi.org/10.1016/j.matdes.2024.113497
Received 5 September 2024; Received in revised form 22 November 2024; Accepted 25 November 2024

and fluorite structures. The distinctive atomic arrangement inherent to each crystalline phase gives rise to a unique set of properties. Rock salt-type HEOs have only one Wyckoff site for cations, which are usually composed of transition metals [18]. The dispersed structure endows rock salt-type HEOs with remarkable chemical stability and reduced thermal conductivity while maintaining their mechanical stiffness [19,20]. The oxygen sublattice in rock salt-type HEOs functions as a buffer layer, mitigating the impact of cationic size differences and leading to the random distribution of metal ions at cationic sites [21]. This structural feature also permits the even distribution of cations with disparate magnetic characteristics within the lattice, whereas the entire system exhibits long-range antiferromagnetic order. The fluorite-type HEOs also have only one Wyckoff site for the cations, which contain mostly rare-earth elements [18]. The single phases of fluorite-type HEOs exhibit lower thermal conductivities than Y_2O_3-doped ZrO_2 does because of the high phonon scattering caused by multiple cations and lattice distortion [22]. Furthermore, they possess superior compatibility with the coefficient of thermal expansion of the metal in comparison to yttria-stabilized zirconia, which is a notable advantage for thermal barrier coating applications [23]. Both spinel and perovskite-type HEOs have multiple Wyckoff sites for cations [18]. The complex unit cell of the spinel structure is composed of 32 anion sites and 24 cation sites, which are arranged in octahedral and tetrahedral cages [24]. This offers significant potential for the development of multicomponent systems. Owing to their multiple electroactive species and rich chemical valance, spinel-type HEOs also achieve excellent Li^+ storage capability and tunable magnetic ordering [24,25]. The magnetic properties of spinel-type thin films have been demonstrated to be amenable to modification through the tailoring of crystallinity and crystalline size, thereby enabling their adaptation to meet the requirements of magnetic recording [26]. Moreover, perovskite-type HEOs have been shown to possess better activities and electrochemical stability than single perovskite oxides do [27]. The magnetic properties of perovskite-type HEOs are significantly influenced by the crystal structure, including lattice distortion and tilting of the BO_6 octahedra [28]. The presence of a multinary transition metal sublattice endows perovskite-type HEOs with both antiferromagnetic and ferromagnetic properties. The competition between these two properties determines the magnetic behavior of the material [28]. However, the multivariate crystal structure presents a significant challenge in the synthesis of materials. The massive number of possible combinations and the effect of each element on the crystal structure render the phase prediction of HEOs a challenging endeavor.

The use of the semi-empirical parameter method to predict the phase stability of HEAs has been extensively studied over the last decade. Researchers have proposed several criteria for the solid solution phase in HEAs on the basis of semi-empirical parameters: (1) the entropy of mixing (ΔS_{mix}) ranges from 12 to $17.5 J \cdot K^{-1} \cdot mol^{-1}$, and the enthalpy of mixing (ΔH_{mix}) ranges from -15 to $5 kJ \cdot mol^{-1}$ [29]; (2) atomic size differences (δ) ≤ 6.6 and Ω-parameter ≥ 1.1 [30]; and (3) valance electron concentration (VEC) values greater than 8 and less than 6.87 are favorable for the stability of face-centered cubic (FCC) and body-centered cubic (BCC) phases, respectively [31]. The intermetallic phase stability of HEAs is greater when the electronegativity difference (ΔX) is greater than 0.133 [32]. Our previous research has provided evidence to support the efficacy of the semi-empirical parameter method for solid solution and intermetallic phases in Co-free HEAs [33,34]. Similarly, several studies have focused on predicting the phase stability of HEOs. Goldschmidt et al. [35] reported a tolerance factor t ($t = (r_A + r_X)/\sqrt{2}(r_B + r_X)$) at which the perovskite phase is prone to be stable when $0.75 \leq t \leq 1.05$. On the basis of the basic unit of the perovskite structure, the octahedron BO_6, another octahedral factor μ ($\mu = r_B/r_O$), was proposed [36]. It was suggested that $0.75 \leq \mu \leq 1.05$ is the range for the formation of the perovskite phase. For the fluorite structure in HEOs, a criterion based on the standard deviation of the constituent cation sizes was proposed [37]. A single-phase fluorite structure can form in HEOs if $s > 0.095$. However, all of the above criteria apply only to specific structures. In addition, the rapid development of HEOs has also created a greater demand for the proposal of simple structure prediction models.

In the present work, for the stability of different HEO structures, simple and general phase stability criteria widely used for HEAs were applied. The semi-empirical parameters, including ΔX, VEC, ΔS_{mix}, ΔH_{mix} and δ, were calculated to determine the phase stability of the rock salt, spinel, perovskite and fluorite structures in HEOs. Two new HEOs were synthesized and characterized to verify their phase stability. In addition, the two new HEOs have also been identified as having the potential to be used as catalysts in wastewater remediation.

2. Methods

2.1. HEO system collection and phase stability criteria

Notably, the criteria for defining high-entropy are not unique and can be classified into two main categories: composition-based definitions and entropy-based definitions [38–40]. The composition-based definition requires that the concentration of each of the principal elements (comprising a minimum of five) that constitute the high-entropy systems falls within the range of 5–35 at.% [6]. Thus, high-entropy systems do not have to have equimolar ratios. Minor elements can also be added to high-entropy systems to tune the microstructure of materials. The criteria have no requirements on the magnitude of entropy or the presence of a single-phase solid solution phase. According to the composition-based definition, nonequimolar quintuple systems with low configurational entropy (minimum value is 1.36R) can also be classified as having high entropy. The entropy-based definition categorizes multicomponent systems with a configurational entropy exceeding 1.61R as high-entropy systems [8]. It is also the case that some of the quaternary equimolar systems are considered to be high-entropy, given that their configurational entropies are higher than the minimum value determined by the composition-based definition [41,42]. The single-phase structure is not a prerequisite in either of the definitions. Since the concept of high entropy in HEOs was introduced from HEAs, the definitions of HEOs are not limited to the initial five equimolar elements or the single phase [22,40,43–45]. Indeed, the concept of high entropy in HEOs has been shown to encompass a broader range of compositions than previously thought.

To reach a compromise between the various definitions and expand the library as much as possible, the collection of HEO systems in this work is governed by the following rules: 1) the multicomponent systems should be composed of 4 or more principal elements; 2) the concentration of each element must exceed 5 at% [40]; and 3) the phase structure should be a single or mixed phase, which contains at least one high-entropy phase. A total of 77 different HEO systems were collected from published literature [14,16,17,20,22,24,43,44,46–61]. The definition of entropy-stabilized oxides has strict requirements. It represents a class of materials with configurational disorder that achieve reversible transformation between a polyphase mixture and a homogeneous solid solution of five binary oxides [9,37]. The solid solutions are inherently unstable when any of the constituents are removed under the same thermal budget [9]. While some HEOs exhibit high configurational entropy, this does not necessarily imply that they are entropy-stabilized systems [15,16]. Notably, the multicomponent systems collected in this work are not all entropy-stabilized systems. Since a reversible transition phenomenon from single-phase to multiphase has been widely observed in HEOs at specific synthesis temperatures [37,62], the phase stability of HEOs can be significantly influenced by the synthesis methods employed [63]. Thus, the list of HEOs should be extended to include multicomponent systems with single or mixed phases, provided that the fraction of secondary phases is small. The compositions, phases and synthesis methods extracted from the literature, as well as the calculated values of the semi-empirical parameters of HEOs, are presented in the Appendix.

The electronegativity difference (ΔX) has been used to determine the phase stability of intermetallic phases in HEAs. It represents the chemical properties of the constituent elements in multicomponent systems. The substantial electronegativity difference between the solute and solvent atoms facilitates the formation of more robust bonds [32]. The definition of ΔX is as follows:

$$\Delta X = \sqrt{\sum\nolimits_{i=1}^{n} C_i (X_i - \overline{X})^2} \tag{1}$$

where C_i and X_i are the atomic fraction and Pauling electronegativity of the i-th element, respectively, and where $\overline{X} = \sum_{i=1}^{n} c_i X_i$ is the average electronegativity in the multicomponent system. The valence electron concentration, VEC, is another electron-related parameter that can reflect the chemical properties of constituent elements. VEC considers the total number of valence electrons, including the electrons partially filled in the d-orbital. It is defined by [31]:

$$VEC = \sum_{i=1}^{n} C_i (VEC)_i \tag{2}$$

where $(VEC)_i$ is the VEC value of the i-th element. The entropy of mixing, enthalpy of mixing and atomic size differences are defined by Eqs. (3), 4 and 5, respectively [29,30]:

$$\Delta S_{mix} = -R \sum_{i=1}^{n} C_i \ln C_i \tag{3}$$

$$\Delta H_{mix} = \sum_{i=1, i \neq j}^{n} \Omega_{ij} C_i C_j \tag{4}$$

$$\delta = 100 \times \sqrt{\sum_{i=1, i \neq j}^{n} C_i (1 - r_i/\overline{r})^2} \tag{5}$$

where R is the gas constant, the i-th element is different from the j-th element; $\Omega = 4\Delta H_{AB}^{mix}$ is the enthalpy of mixing between the interacting elements i and j, which is considered the interaction between two adjacent constituent cations in multicomponent systems; r_i is the atomic radius of the i-th element; and $\overline{r} = \sum_{i=1}^{n} c_i r_i$ is the average atomic radius of HEOs.

Given that the anion exerts a constrained influence on the configurational entropy of HEOs, ΔS_{mix} is determined on the basis of the proportion of cations. The ΔH_{mix} is also based on the interaction between cations. In HEOs, cations exhibit distinct oxidation states and cationic radii at different cation sites. To facilitate the calculation process, the value of δ is based on the atomic radii.

2.2. Experimental details

All chemical agents, including potassium ferricyanide ($K_3[Fe(CN)_6]$), potassium hexacyanocobaltate ($K_3[Co(CN)_6]$), copper(II) acetate monohydrate ($Cu(Ac)_2 \cdot H_2O$), trisodium citrate dihydrate ($Na_3C_6H_5O_7 \cdot 2H_2O$), nickel(II) acetate tetrahydrate ($Ni(Ac)_2 \cdot 4H_2O$), and manganese(III) acetate dihydrate ($Mn_2(Ac)_3 \cdot 2H_2O$), were obtained from Macklin Biochemical.

PBAs (Prussian blue analogs) were first prepared as precursors through a facile coprecipitation method. Typically, a certain amount of ($Cu(Ac)_2 \cdot H_2O$), ($Ni(Ac)_2 \cdot 4H_2O$), or $Na_3C_6H_5O_7 \cdot 2H_2O$ was added to 100 mL of ultrapure water, and solution A was marked. $K_3[Co(CN)_6]$ and $K_3[Fe(CN)_6]$ were subsequently dissolved in 40 mL of ultrapure water, and solution B was marked. Then, solution B was added dropwise, and the mixture was continuously stirred for 1 h. The obtained suspension was left at room temperature for a certain time. After being washed with deionized water and ethanol and dried overnight at 60 °C, the PBAs were obtained. Finally, the PBAs were further annealed under an air atmosphere, and HEO-Cu and HEO-Mn were obtained. The amounts of raw materials used are listed in detail in Table 1.

The phase structure of the samples was studied via Smartlab 3 X-ray diffraction (XRD) with a Cu $K\alpha$ radiation source and a Talos F200X transmission electron microscope (TEM). The chemical compositions were studied via X-ray photoelectron spectroscopy (XPS, Thermo-Scientific ESCALAB 250xi spectrometer) and scanning electron microscopy (SEM, Regulus 8100 field) with energy dispersive X-ray spectroscopy (EDS).

For the test of wastewater remediation application, peroxymonosulfate (PMS, 0.5 mM, Macklin Biochemical) and methyl orange (MO, Macklin Biochemical) were selected as the oxidizing agent and target pollutant, respectively. Specifically, the powder material (100 ppm) was uniformly dispersed in the MO solution (50 ppm), and the obtained suspension was stirred for 1 h to achieve adsorption–desorption equilibrium. Then, PMS was added to start the catalytic process, 3 mL of the suspension was removed within a given time, mixed with excess sodium thiosulfate ($Na_2S_2O_3$, Macklin Biochemical) to terminate the reaction, and filtered with a 0.22 μm filter membrane. Finally, the absorbance of the supernatant was measured with a Cary UV–Vis spectrophotometer at 464 nm. All degradation experiments were carried out in a 25 °C constant-temperature water bath.

3. Results

3.1. Performance of various structures on five parameters

The effects of the semi-empirical parameters ΔX, VEC, ΔS_{mix}, ΔH_{mix} and δ on the stability of rock salt, spinel, perovskite and fluorite structures are plotted in Fig. 1. The values of ΔX for rocaksalt, spinel and perovskite have similar distributions, as shown in Fig. 1a. The ΔX values of perovskite are slightly higher than those of rock salt, whereas the counterparts of spinel exhibit a wide distribution range. Fluorite, however, displays a markedly low ΔX value. A comparable phenomenon is observed in the case of VEC, as shown in Fig. 1b. The maximum value of VEC in fluorite is lower than that observed in rock salt, spinel and perovskite. The VEC values of rock salt and spinel have analogous distributions, whereas the VEC values of perovskite are relatively lower among these three structures. The ΔS_{mix} values, which are calculated via the configurational entropy of HEAs, are relatively randomly distributed, as shown in Fig. 1c. The ΔS_{mix} values of the perovskites are only two distinct values: 12.45 and 19.14 $J \cdot K^{-1} \cdot mol^{-1}$. For the ΔHmix in Fig. 1 d, fluorite has higher values than the counterparts of the other three structures. The highest values of δ are observed in the perovskite, as shown in Fig. 1e. In light of the aforementioned observations, a single parameter is insufficient for distinguishing the distribution ranges of the four structures. A more comprehensive comparison is needed.

3.2. Performance of multiparameter combination

The important role of atomic size differences δ in the phase stability of multicomponent systems has been discussed in the fields of HEAs and ceramics [64,65]. Therefore, the maps combining δ with ΔX, VEC, ΔS_{mix} and ΔH_{mix} are plotted in Fig. 2 to show the comprehensive effect of multiple parameters on phase stability.

The $\Delta X - \delta$ map in Fig. 2a shows that the rock salt, perovskite and fluorite structures are distributed independently in three distinct regions. The fluorite and perovskite structures exhibit the lowest and highest values of ΔX and δ, respectively, among the four structures under consideration. The ΔX values of the rock salt structure are similar to those of the perovskite structure, whereas its δ values are between those of the fluorite and perovskite structures. The distribution of the spinel structure is divided into two regions. One region is analogous to rock salt, exhibiting high ΔX and medium δ values, whereas the other displays lower ΔX and δ *values*, akin to a fluorite structure. Similar distributions of rock salt and spinel structures are observed in the $VEC - \delta$ map. The

Table 1
The detailed amounts of agents used for the preparation of HEO-Cu and HEO-Mn.

Samples	$K_3[Fe(CN)_6]$	$K_3[Co(CN)_6]$	$Mn_2(Ac)_3{\cdot}2H_2O$	$Ni(Ac)_2{\cdot}4H_2O$	$Cu(Ac)_2{\cdot}H_2O$	$Na_3C_6H_5O_7{\cdot}2H_2O$	Temperature
HEO-Cu	1.6463 g	1.6617 g	–	1.2442 g	0.9983 g	1.5000 g	300 °C
HEO-Mn	0.0660 g	0.0660 g	1.0724 g	0.7460 g	–	2.0587 g	500 °C

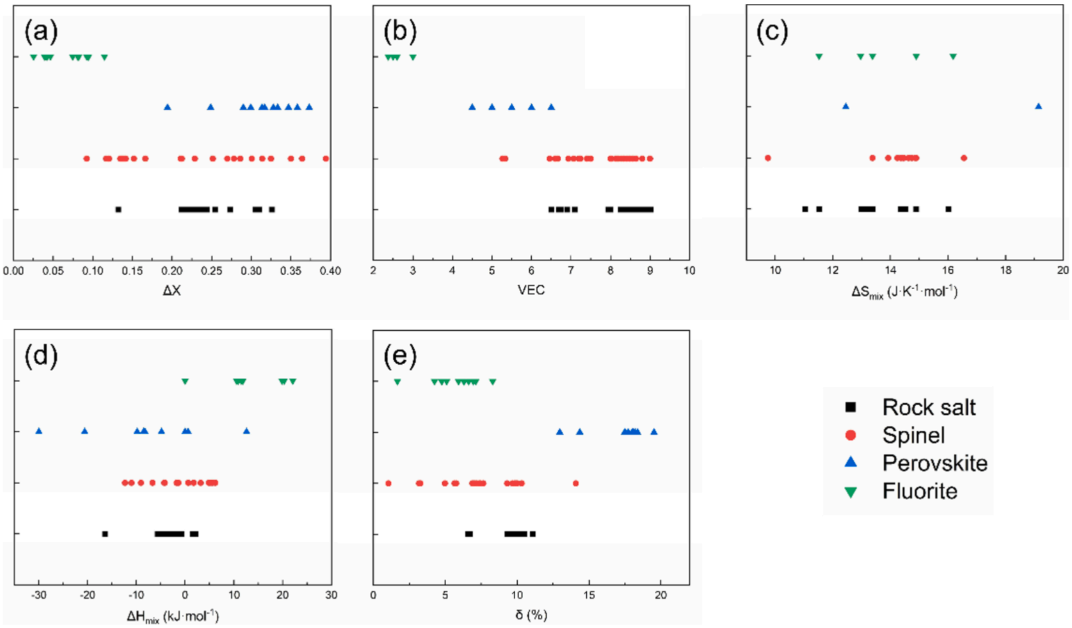

Fig. 1. Effects of (a) ΔX, (b) VEC, (c) ΔS_{mix}, (d) ΔH_{mix} and (e) δ on phase stability in HEO.

fluorite structure has the lowest VEC values, whereas the perovskite structure is located in the middle region. The fluorite and perovskite structures can be distinguished from the rock salt and spinel structures in the $VEC - \delta$ map. It is difficult to differentiate between various structures on the basis of ΔS_{mix} alone. The distributions of fluorite, rock salt and perovskite structures become apparent *only when* ΔS_{mix} *and* δ *are combined*, as illustrated in Fig. 2c. The distribution region of the spinel structure is contiguous with that of the fluorite and rock salt structures. As illustrated in the $\Delta H_{mix} - \delta$ map in Fig. 2d, the fluorite, rock salt and perovskite structures are also distributed across three distinct regions. The distribution of spinel overlaps with that of rock salt and some fluorite structures.

To gain a more accurate understanding of the impact of semi-empirical parameters on the phase stability of HEOs, additional combined maps have been plotted. Fig. 3 shows the combined maps of $VEC - \Delta X$ and $\Delta H_{mix} - \Delta S_{mix}$. The rock salt, perovskite and fluorite structures are distributed in three distinct regions in the $VEC - \Delta X$ map. The distribution of spinel is more extensive. The distribution region of the spinel structure encompasses the rock salt structure to a significant extent. The distributions of rock salt, perovskite and fluorite structures partially overlap in the $\Delta H_{mix} - \Delta S_{mix}$ map. Despite the proven efficacy of the $\Delta H_{mix} - \Delta S_{mix}$ map in predicting the phase stability of HEAs, this approach remains challenging for the determination of structures in HEOs.

Owing to the inefficiency of ΔS_{mix} in determining the phase stability of HEOs, the maps of ΔH_{mix} combined with ΔX and VEC are presented in Fig. 4 for illustrative purposes. In the $\Delta H_{mix} - \Delta X$ map, only the fluorite structure can be distinguished from the other three structures. The distribution of the spinel structure completely overlaps with that of the rock salt structure and partially overlaps with that of the perovskite structure. A similar distribution is observed in the $\Delta H_{mix} - VEC$ map. The regions of the rock salt, spinel and perovskite structures overlap. Among the four structures, the distribution of the fluorite structure is the most obviously different.

On the basis of the aforementioned observations, it is possible to propose ranges of five parameters for the stability of each structure. It is more stable for the rock salt structure when $0.132 \leq \Delta X \leq 0.326$, $6.50 \leq VEC \leq 9.02$, $-16.40 \leq \Delta H_{mix} \leq 2.11$ kJ·mol^{-1} and $6.60 \leq \delta \leq 11.08$ %; the ranges for the spinel structure are $0.092 \leq \Delta X \leq 0.394$, $5.27 \leq VEC \leq 9.00$, $-12.32 \leq \Delta H_{mix} \leq 6.19$ kJ·mol^{-1} and $\delta \leq 14.09$ %; the ranges for the perovskite structure are $0.194 \leq \Delta X \leq 0.373$, $4.50 \leq VEC \leq 6.50$, $-30.00 \leq \Delta H_{mix} \leq 12.60$ kJ·mol^{-1} and $12.97 \leq \delta \leq 19.52$ %; and the ranges for the fluorite structure are $0.025 \leq \Delta X \leq 0.115$, $2.38 \leq VEC \leq 3.00$, $0.00 \leq \Delta H_{mix} \leq 22.08$ kJ·mol^{-1} and $1.67 \leq \delta \leq 8.30$ %.

3.3. Phase stability of the HEOs

To further verify the rationality of the above observations, two kinds of new HEOs were designed, and their phase compositions were also researched. A new HEO containing Fe, Co, Ni, and Cu was obtained through a facile two-step method. In addition, another Mn-containing HEO, which is quite different from the electronegativity of three common elements (Fe, Co, and Ni), was selected from previous research to further verify other parameters (such as ΔX). The compositions of the two new HEOs and the corresponding values of the parameters are shown in Table 2. After the composition analysis, HEO-Cu and HEO-Mn were determined to be $(Fe_{0.1}Co_{0.19}Ni_{0.4}Cu_{0.31})_3O_4/CuO$ and $(Fe_{0.18}Co_{0.19}Ni_{0.31}Mn_{0.32})_3O_4/MnO_2$, respectively. These two new HEOs are designed to be within the range of the spinel structure, which is outside the ranges of the other three structures, as shown in Fig. 5. According to the determined phase stability and compositional design, $(Fe_{0.1}Co_{0.19}Ni_{0.4}Cu_{0.31})_3O_4/CuO$ and $(Fe_{0.18}Co_{0.19}Ni_{0.31}Mn_{0.32})_3O_4/MnO_2$ should have a spinel structure.

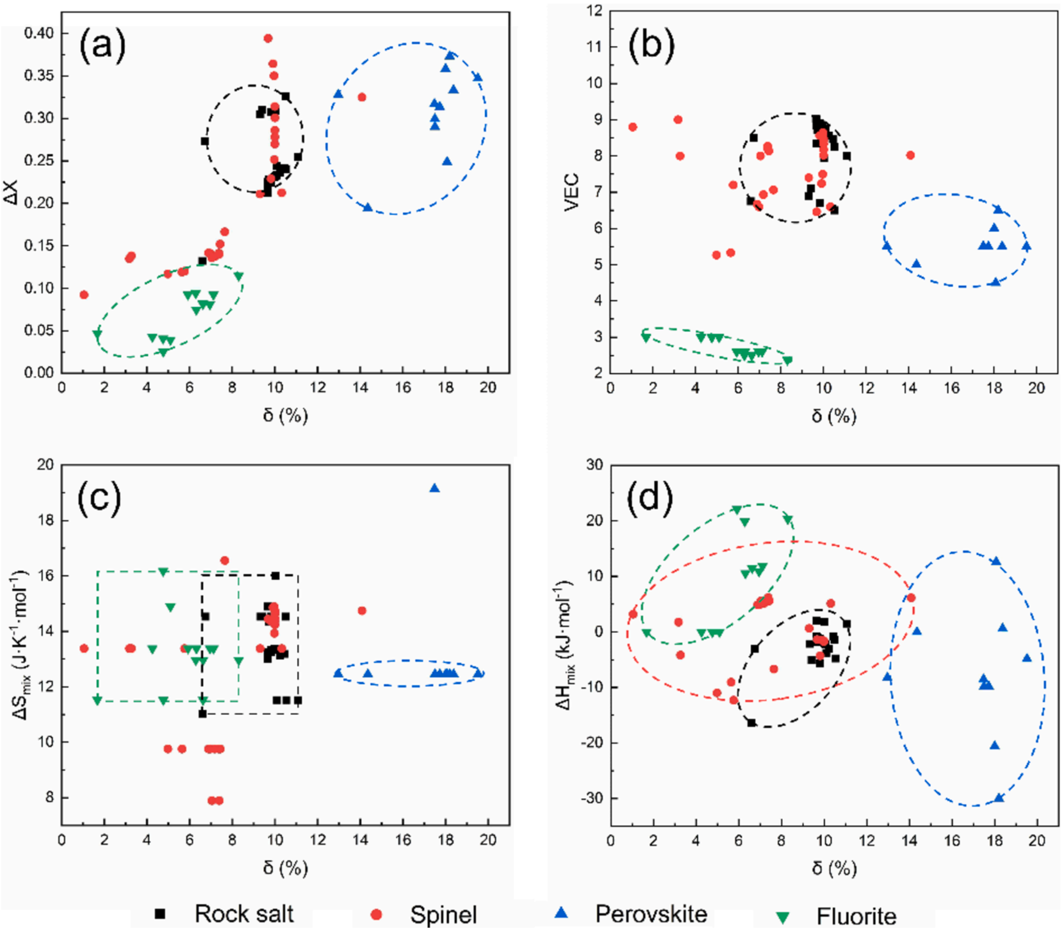

Fig. 2. Distributions of δ superimposed with parameters (a) ΔX, (b) VEC, (c) ΔS_{mix} and (d) ΔH_{mix}. (The distribution of structures is indicated by dashed lines of corresponding colors, with the exception of points and structures that are overdispersed.).

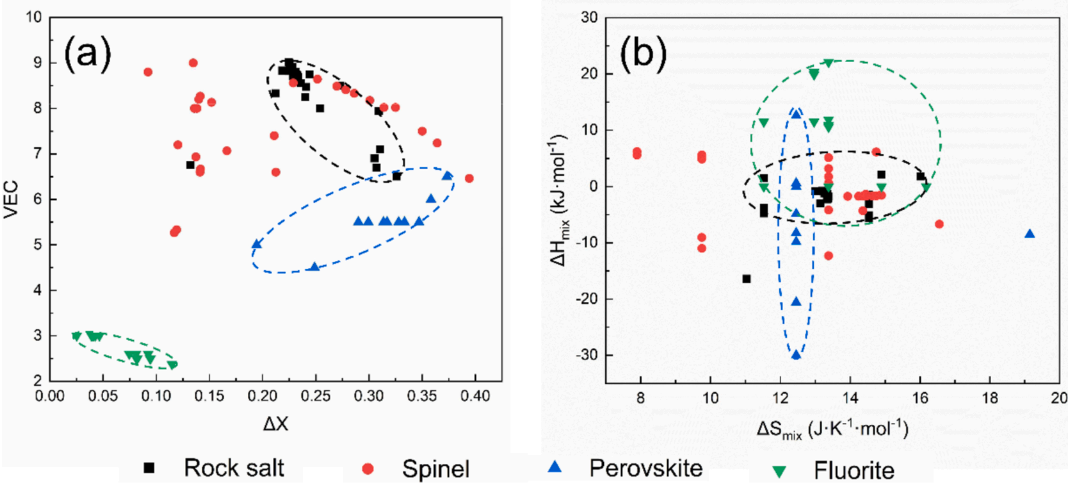

Fig. 3. Binary factor maps: (a) $VEC - \Delta X$ and (b) $\Delta H_{mix} - \Delta S_{mix}$.

3.4. Characterization of the HEOs

The phase stability of HEOs proposed in this work requires verification through examination of the phase structures of the newly designed HEOs $(Fe_{0.1}Co_{0.19}Ni_{0.4}Cu_{0.31})_3O_4/CuO$ and $(Fe_{0.18}Co_{0.19}Ni_{0.31}Mn_{0.32})_3O_4/MnO_2$. X-ray diffraction (XRD) and transmission electron microscopy (TEM) were employed to characterize the phase structure of the as-prepared HEOs further, as shown in Figs. 6 and 7.

The XRD pattern of $(Fe_{0.1}Co_{0.19}Ni_{0.4}Cu_{0.31})_3O_4/CuO$ is shown in Fig. 6a. In addition to the spinel phase (JCPDS No. 88–1937) [66], there are diffraction peaks that correspond to the CuO phase (JCPDS No. 80–1917) [67]. Moreover, as depicted in Fig. 6b, two different morphologies, bulks (bottom-left) and particles (top-right), of the sample are observed in the TEM image. The corresponding selected area electron

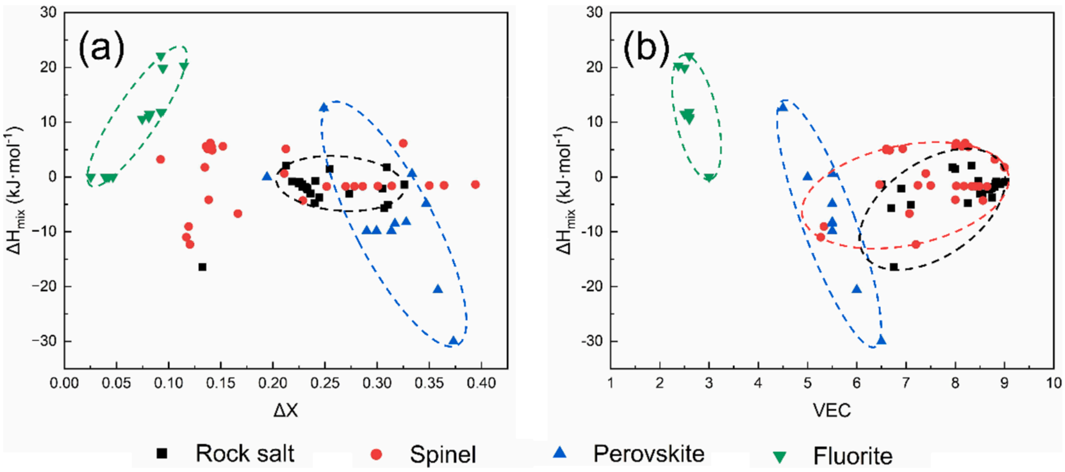

Fig. 4. Binary factor maps: (a) $\Delta H_{mix} - \Delta X$ and (b) $\Delta H_{mix} - VEC$.

Table 2
The composition (at.%) and parameter values of HEOs.

Samples	Fe	Co	Ni	Cu	Mn	*ΔX*	*VEC*	ΔS_{mix} ($J \cdot K^{-1} \cdot mol^{-1}$)	ΔH_{mix} ($kJ \cdot mol^{-1}$)	*δ* (%)
HEO-Cu	10.2	19.0	39.6	31.2	–	0.024	9.92	10.63	4.65	1.14
HEO-Mn	17.9	19.2	31.1	–	31.8	0.156	8.50	11.24	−4.97	3.79

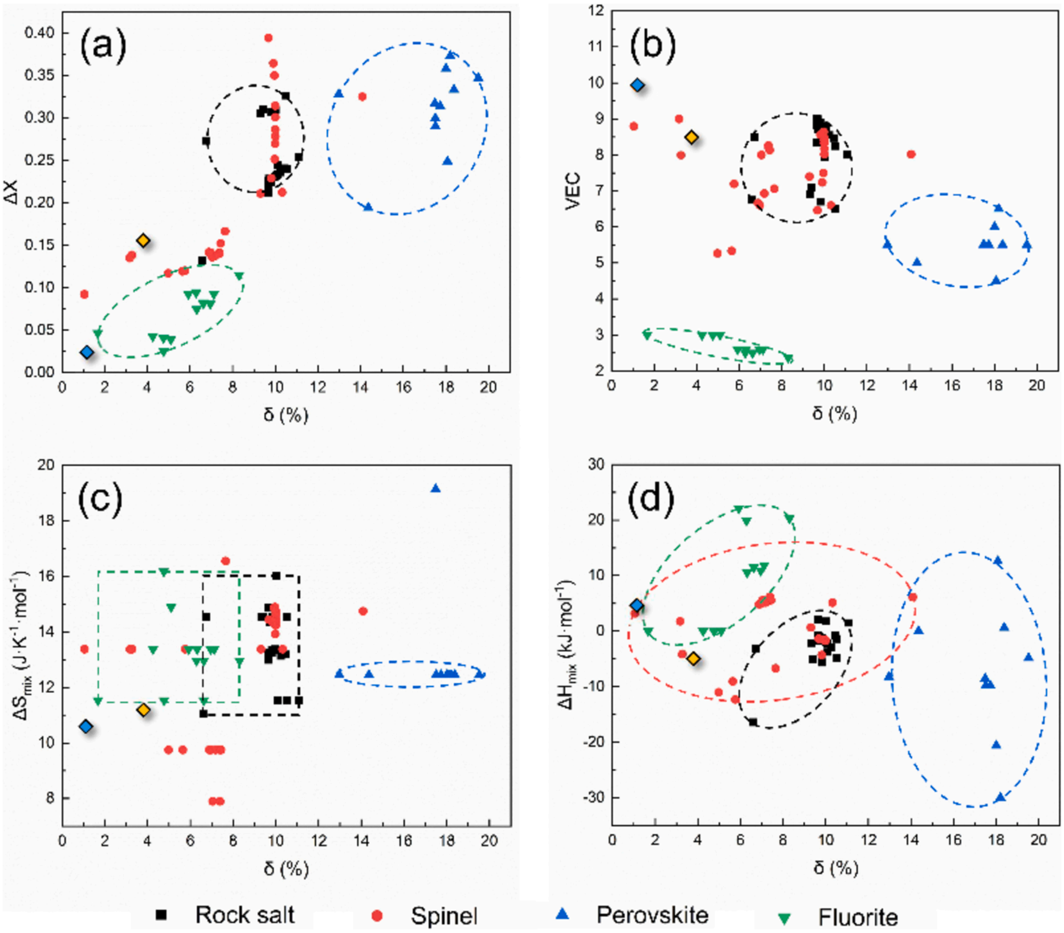

Fig. 5. The updated maps of Fig. 2 include the new HEO-Cu (blue rhombus) and HEO-Mn (yellow rhombus).

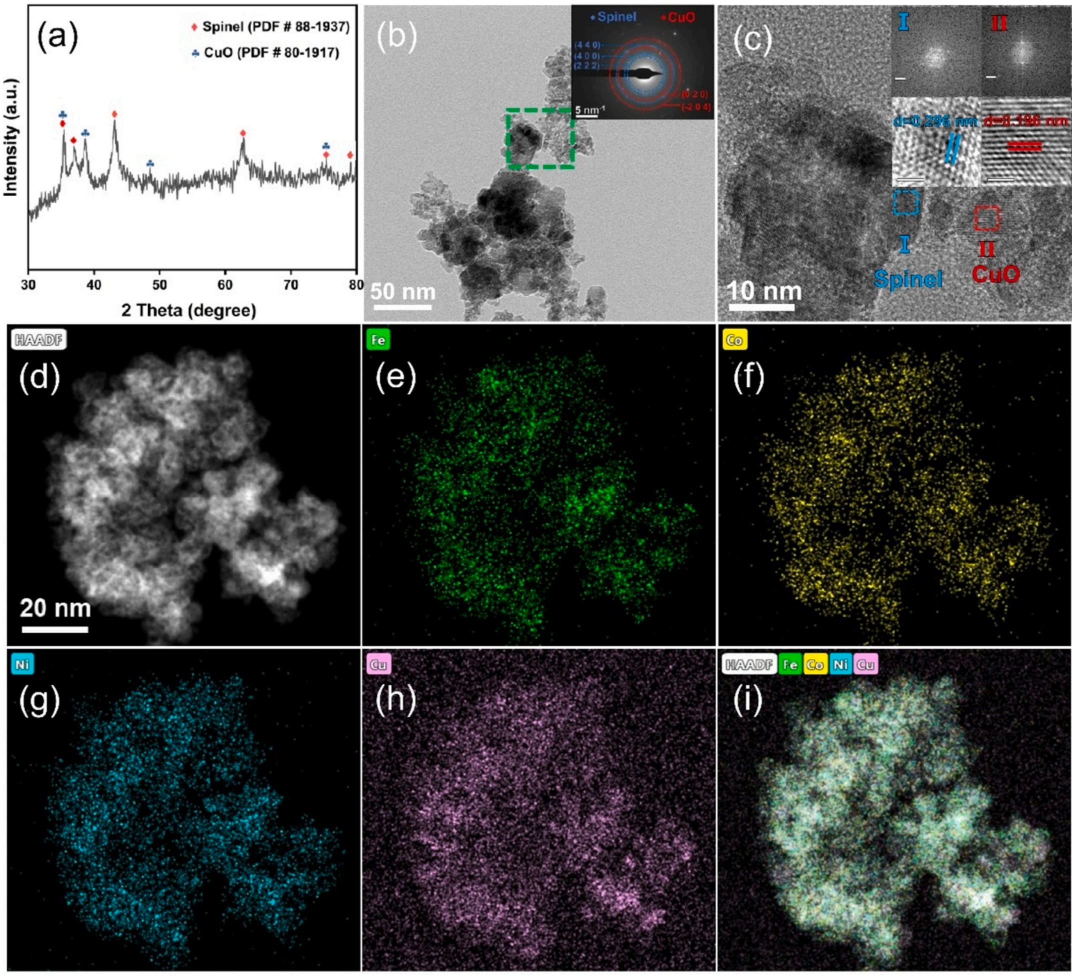

Fig. 6. (a) XRD pattern, (b) TEM image and SAED patterns (inset), (c) HRTEM results (inset: the corresponding FFT and IFFT patterns of the selected zone), (d) HAADF image, and (e)-(i) EDS mapping results of HEO/CuO.

diffraction (SAED) pattern indicates the polycrystalline characteristic and exhibits two sets of diffraction patterns of the sample, which correspond to spinel (blue) and CuO (red). On the other hand, Fig. 6c shows a high-resolution TEM (HRTEM) image, which was obtained by locally amplifying the TEM image (green dotted line marked area). The insets in Fig. 6c show the corresponding fast Fourier transform (FFT) and inverse fast Fourier transform (IFFT) of the selected areas. The lattice spacing of the sample with the bulk morphology (region I) is 0.296 nm, which is attributed to the (220) plane of the spinel. Moreover, the particle sample (region II) with a spacing lattice of 0.196 nm corresponds to the (_112) plane of CuO. Furthermore, to determine the element compositions of the as-prepared sample, STEM-EDS was employed, as shown in Fig. 6d-f. Metal elements, including Fe, Co, Ni, and Cu, coexist in the HEO. In particular, a wider distribution of Cu can be observed than other metal elements in Fig. 6i, indicating the special precipitation characteristics of Cu.

On the basis of the above discussion, HEO containing Fe, Co, Ni, and Cu is considered to be composed of spinel and copper oxide phases. This can be attributed to the difference in ΔH_{mix} values between these elements ($\Delta H_{mix\ (\text{Fe-Ni})} = -2$, $\Delta H_{mix\ (\text{Fe-Cu})} = 13$, $\Delta H_{mix\ (\text{Co-Ni})} = 0$, $\Delta H_{mix\ (\text{Fe-Co})} = -1$, $\Delta H_{mix\ (\text{Co-Cu})} = 6$, $\Delta H_{mix\ (\text{Ni-Cu})} = 4$) [68]. In particular, the ΔH_{mix} values of Cu and the other three elements are positive, which means that a high ΔH_{mix} of FeCoNiCu-based HEOs is immiscible with Fe, Ni, and Co. Therefore, during heat treatment of the FeCoNiCu PBA precursor, in addition to the formation of a spinel phase of HEO, the immiscible Cu tends to precipitate on the HEO surface and form CuO under an air atmosphere.

The structural characterization of $(Fe_{0.18}Co_{0.19}Ni_{0.31}Mn_{0.32})_3O_4/MnO_2$ is illustrated in Fig. 7. The XRD results of the sample indicated that the sample was composed of two different phases (Fig. 7a). Specifically, most of the diffraction peaks could correspond to the standard card (JCPDS No. 88–1937) [66] of the spinel phase. However, the peaks at 12.5° and 25.2° completely match the (001) and (002) crystal planes of MnO_2 [69], indicating the formation of the second phase of MnO_2. This conclusion is also verified by the related TEM, SAED, and HRTEM results. Two morphologies with obviously distinct scales can be observed in Fig. 7b. The related SAED pattern also shows two different sets of polycrystalline diffraction rings, corresponding to the (440), (400), and (222) planes of the spinel phase (blue) and the (222) and (_204) planes of MnO_2 (green). Moreover, two different regions are selected in the HRTEM image, as depicted in Fig. 7d. The lattice spacing of Region I obtained from the FFT and IFFT in Fig. 7d is 0.484 nm, which corresponds to the (1 1 1) plane of the spinel phase, whereas that of Region II is 0.247 nm, matching the (1 1 0) plane of the MnO_2 phase. Therefore, it is reasonable to believe that the HEO composed of Fe, Co, Ni, and Mn is composed of spinel and MnO_2 phases. This is mainly due to the electronegativity difference between Mn and the other three elements (Fe, Co, and Ni) and the large ΔX value, which allows Mn to easily precipitate to form the second phase MnO_2 during the synthesis of the FeCoNiMn-based HEO.

Additionally, the XRD peaks of the two HEOs have different intensities, as shown in Fig. 6a and 7a. The intensity differences of the peaks between the two HEOs can be caused by the composition variation. The (444) peak at approximately 80° is frequently observed in the

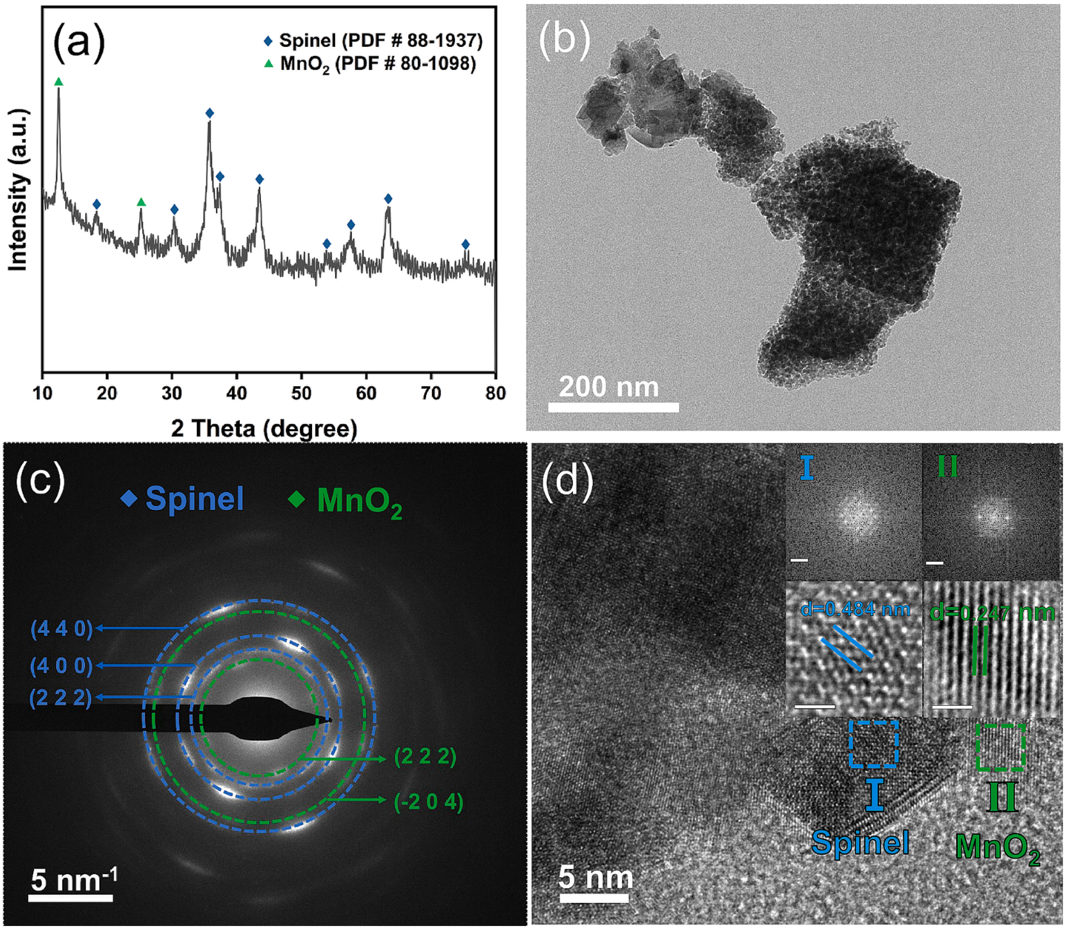

Fig. 7. (a) XRD pattern, (b) TEM image, (c) SAED patterns (inset), (d) HRTEM image with the corresponding FFT and IFFT patterns of HEO/MnO_2.

Cu-containing spinel structure, whereas the (422) peak at approximately 55° is relatively weak [44,52]. In contrast, some Mn-containing spinel structures have strong (422) peaks [25,26,70]. The synthesis of high-entropy alloy systems and high-entropy selenides derived from PBAs has been reported [71,72]. A series of multicomponent oxides, such as CoNiCuMnZnFe-oxide, were synthesized via the thermal treatment of PBA by Du et al. [73]. Despite the absence of a definitive delineation of HEOs derived from high-entropy PBAs, the two oxide systems developed in this study can be identified as HEOs on the basis of various studies on the concept of high entropy and the definition of HEO outlined previously. The microstructure characterization of HEOs reveals the presence of mixed phases, comprising a primary spinel phase and secondary phases of CuO/MnO. The results demonstrate that the desired phase in HEO can be achieved through the utilization of the phase stability diagrams proposed in the present study.

The complex composition of HEOs lends them value in a multitude of potential applications, such as optics [74], energy storage [75–78] and catalysis [79,80]. The potential of HEOs as catalysts for the remediation of wastewater is attracting increasing attention as a result of ongoing efforts to protect the environment [81–83]. The application of HEO/CuO and HEO/MnO_2 for wastewater remediation was further evaluated. On the one hand, these materials have been applied as catalysts in advanced oxidation systems (AOPs) for wastewater treatment. As shown in Fig. 8a, MO was only removed by ~ 2.0 %, 2.2 %, and 30.1 % when

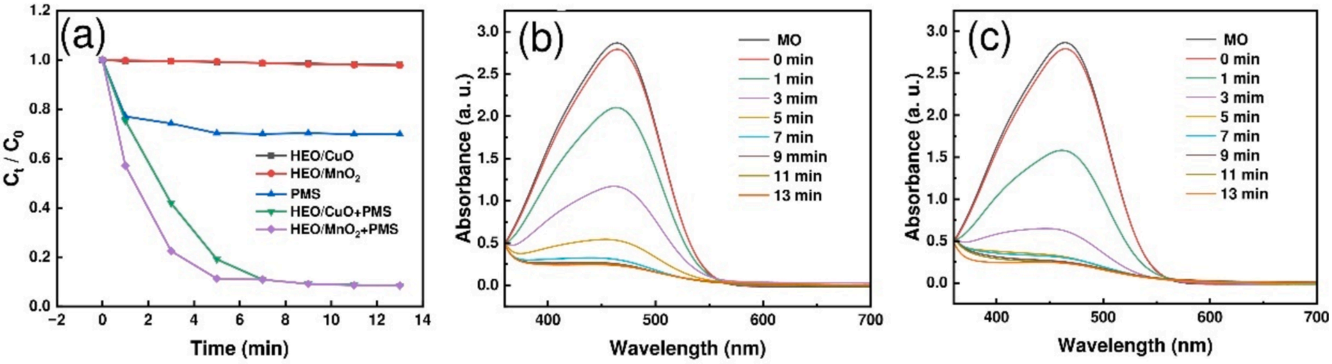

Fig. 8. (a) Time-dependent degradation curves for MO with different systems. UV–visible absorption spectra of MO at different catalytic times in the HEO/MnO_2 + PMS (b) and HEO/MnO_2 + PMS (c) systems.

the HEO/CuO, HEO/MnO_2, and PMS catalysts were present alone, indicating the low contribution of catalyst adsorption and PMS oxidation to the degradation of pollution. When HEO/CuO and HEO/MnO_2 were added to the PMS system, the systems could degrade 92.7 % and 92.5 % of the MO, respectively, which verified that the catalyst can efficiently catalyze PMS to achieve pollutant removal. In addition, as shown in the UV–visible absorption spectrum in Fig. 8b-c, MO presented a maximum absorption wavelength of 464 nm. In the HEO/MnO_2 + PMS and HEO/MnO_2 + PMS systems, with increasing catalytic time, the intensity of the absorption peaks decreased continuously, which further confirmed the effective removal of pollutants. The above results verified that the prepared HEO/MnO_2 and HEO/MnO_2 have broad application prospects in the fields of environment and energy. In the future, more HEOs with specific structures can be synthesized to evaluate their functional applications.

4. Discussion

The collective effect of multiple semi-empirical parameters on the phase stability of HEOs indicates that the atomic size difference δ is the most efficient factor in determining the phase structure. In accordance with the Hume-Rothery rules, the equilibrium of solid solution phases in binary alloys is not constant because of the considerable influence of δ [84]. The excess δ hinders the diffusion of atoms and results in the disruption of the cation distribution disorder [30,33,85]. Various ceramic phases have different tolerances to δ because of their different crystal structure characteristics. The lattice distortion resulting from an increase in δ causes a phase structure to transition from one stable state to another [65,86–88]. As illustrated in Fig. 1, a portion of the HEOs retain a stable phase structure despite the considerable δ values, particularly in the case of the perovskite structure. This study demonstrates that the combination of δ with other parameters still offers valuable insights. Among the five parameters, ΔS_{mix} has the least significant influence on the phase structure of HEOs. This may be attributed to the fact that HEOs possess considerable configurational entropy, which results in negligible variation in ΔS_{mix} energy across disparate phase structures [89]. Furthermore, the majority of HEOs are composed of elements in equimolar ratios, as listed in Table. A1, which also constrains the distribution range of the ΔS_{mix} values. A similar finding was reported by Liu et al. for the crystal structure prediction of high-entropy oxide ceramics [90]. Djenadic et al. [16] studied the role of configurational entropy in the stability of the (Ce, La, Pr, Sm, Y)$O_{2-\delta}$ system by heat treatment at different temperatures. No reversible single-to-multiple-phase transition driven by entropy was identified; thus, the value of configurational entropy is not the main factor determining phase stability. The aforementioned parameters reflect disparate aspects of the performance of HEOs, thereby engendering disparate effects on phase stability.

In previous studies, ΔX and ΔH_{mix} were found to play crucial roles in determining the formation of stable AlB_2-type high-entropy borides [91]. The electronegativity difference, ΔX, is an important indicator for measuring atomic bonding and can directly determine the structural stability of compounds. A value of ΔX that is either too large or too small results in structural instability and the formation of multiple phases in high-entropy borides. In a further report on the phase prediction of high-entropy carbides, it was also demonstrated that the stability of carbides with a rock salt structure is sensitive to ΔX [92]. It was suggested that a small electronegativity difference impedes the formation of a stable high-entropy lattice. The ΔX values of the fluorite structure are lower than those of the rock salt, spinel and perovskite structures. This is attributed to the constituent elements of the fluorite structure, and the involved rare-earth metals include La, Ce, Y, Gd, Pr, Nd and Sm. The Pauling electronegativity values of these elements exhibit a relatively narrow range of variation, with a maximum difference of 0.12 observed in Nd and La [39]. To achieve an entropy-stabilized phase in HEOs, considering the enthalpy of mixing as a critical factor is essential. A low ΔH_{mix} value is usually necessary to ensure that the negative Gibbs free energy of mixing can be obtained [93]. Nevertheless, some HEOs display large and positive ΔH_{mix} values and sustain a relatively stable phase, as observed in Fig. 1. In the case of nonequiatomic high-entropy systems containing specific cations, such as Cu^{2+} and Zn^{2+}, with high positive ΔH_{mix} values [9], it is necessary for the ΔS_{mix} to be positive and of a sufficient magnitude to ensure that the Gibbs free energy of the solid solution phase is negative ($\Delta G_{mix} = \Delta H_{mix} - T\Delta S_{mix}$) [44,65], thereby facilitating its formation. If ΔS_{mix} is insufficient for a negative Gibbs free energy in a nonequiatomic high-entropy system, thermodynamic instability of the solid solution phase can occur. It is thus necessary to tune the component of the nonequiatomic high-entropy system to achieve a large and positive ΔS_{mix}.

It is therefore evident that a reduction in ΔH_{mix} cannot be employed as a means of achieving phase stabilization through the removal of the aforementioned cations with positive enthalpy. These HEOs with positive enthalpies require high temperatures ($T\Delta S_{mix}$) to obtain a negative Gibbs free energy. For example, the synthesis temperature of $(Hf_{0.2}Zr_{0.2}Ce_{0.2})(Yb_{0.2}Gd_{0.2})O_{2-\delta}$ and $(Hf_{0.2}Zr_{0.2}Ce_{0.2})(Y_{0.2}Yb_{0.2})O_{2-\delta}$ is 1800 °C, which is the highest value of ΔH_{mix} among the systems under consideration [22]. In the synthesis of phase-stable HEOs with positive enthalpy, it is particularly important to consider the appropriate temperature and configurational entropy.

The chemical bonding types of HEOs are diverse and include covalent, ionic, and metallic bonds [94]. The ionic and covalent bonds between cations and anions inevitably result in the formation of short-range ordered structures due to the increased bond strength of these bonds [93]. The configurational entropy is thus reduced by the influence of ionic and covalent bonds. The valence electron concentration (*VEC*) is a measure of the valence number of the constituent metals in HEOs and can be used as an indicator of metallic bonds [94]. A *VEC* value that is insufficiently high will result in the destruction of structural disorder, thereby rendering the attainment of a high entropy effect unfeasible. Alternatively, an elevated *VEC* value also results in phase instability. Balasubramanian et al. [95] reported the effects of *VEC* on the mechanical properties of nitrides, carbides and carbonitrides with rock salt structures. The rock salt structure becomes unstable when the *VEC* value exceeds 10.5. This is closely related to the *d*-orbital hybridization state of the constituent elements, as reflected by the *VEC*. The mechanical properties of HEOs are also significantly affected by the phase stability, as indicated by *VEC*. The toughness of high-entropy ceramic materials can be enhanced within a specific range by *VEC* [96,97]. Therefore, to facilitate the design of high-performance HEOs, determining the *VEC* range for phase stability is highly important.

In addition, the rock salt, perovskite and fluorite structures are distributed across three distinct regions in the majority of the maps, as illustrated in Figs. 2 and 3. Nevertheless, the semi-empirical parameter ranges of the spinel structure are evidently more extensive, and the corresponding distribution in the maps is considerably more dispersed. The phase stability of the spinel structure is indistinguishable from that of the other structures, particularly the rock salt structure, in all the maps. This phenomenon has also been documented in other studies [90]. This may be attributed to the distinctive characteristics of the spinel structure, which renders semi-empirical parameters ineffective in accurately predicting its phase stability. Further investigations are needed to gain a deeper understanding of the phase stability of the spinel structure.

The semi-empirical method provides a straightforward tool for researchers to perform initial composition design. The combination of the semi-empirical method with newer composition space exploration methods has the potential to significantly enhance the prediction of phase stability. The high-throughput (HT) experimental method is a convenient approach for examining the phase stability of complex multicomponent systems [98–103]. Kumbhakar et al. used the HT method to examine the phase structure of CeLaSmPrTbYZr-oxide systems with fluorite structures [104]. A decrease in the number of components in multicomponent systems can significantly deteriorate the stability of the fluorite structure. This report aligns well with the findings of the present work, in which the majority of fluorite-type HEOs listed in Table A1 present configurational entropy values exceeding 1.5R, i.e., ~12.47 $J\cdot K^{-1}\cdot mol^{-1}$. However, HT methods are usually used for the measurement of selected multicomponent systems. The proposed phase stability diagrams include the vast majority of multicomponent systems that have been reported. Furthermore, it enables researchers to make preliminary assessments of the phase stability of novel compositions. In the future, the combined use of phase stability diagrams and HT methods will make it easier and faster to design and test the composition of new materials.

5. Conclusions

In this work, five semi-empirical parameters, ΔX, VEC, ΔS_{mix}, ΔH_{mix} and δ, of various HEO systems were carefully calculated to determine the phase stability of the rock salt, spinel, perovskite and fluorite structures. The maps of δ superimposed with ΔX, VEC and ΔH_{mix} are efficient indicators for determining the phase stability of rock salt, perovskite and fluorite structures. ΔS_{mix} does not appear to have a significant effect on the phase stability of these four structures on the basis of the current database. The distribution of spinel in all maps is observed to be scattered. The results partially overlap with the range of rock salt structures identified via semi-empirical methods. The phase stability ranges determined by the semiempirical parameters are as follows: the ranges for the rock salt structure are $0.132 \leq \Delta X \leq 0.326$, $6.50 \leq VEC \leq 9.02$, $-16.40 \leq \Delta H_{mix} \leq 2.11$ $kJ\cdot mol^{-1}$ and $6.60 \leq \delta \leq 11.08$ %; the ranges for the spinel structure are $0.092 \leq \Delta X \leq 0.394$, $5.27 \leq VEC \leq 9.00$, $-12.32 \leq \Delta H_{mix} \leq 6.19$ $kJ\cdot mol^{-1}$ and $\delta \leq 14.09$ %; the ranges for the perovskite structure are $0.194 \leq \Delta X \leq 0.373$, $4.50 \leq VEC \leq 6.50$, $-30.00 \leq \Delta H_{mix} \leq 12.60$ $kJ\cdot mol^{-1}$ and $12.97 \leq \delta \leq 19.52$ %; and the ranges for the fluorite structure are $0.025 \leq \Delta X \leq 0.115$, $2.38 \leq VEC \leq 3.00$, $0.00 \leq \Delta H_{mix} \leq 22.08$ $kJ\cdot mol^{-1}$ and $1.67 \leq \delta \leq 8.30$ %. The new HEOs $(Fe_{0.1}Co_{0.19}Ni_{0.4}Cu_{0.31})_3O_4/CuO$ and $(Fe_{0.18}Co_{0.19}Ni_{0.31}Mn_{0.32})_3O_4/MnO_2$, which exhibit mainly a spinel structure, serve to verify the phase stability determined in this work. Moreover, the two new HEOs demonstrated utility as catalysts because of their ability to remediate wastewater.

CRediT authorship contribution statement

Yulin Li: Writing – original draft, Visualization, Investigation, Formal analysis. **Haixian Yan:** Writing – original draft, Visualization, Investigation. **Shiqi Wang:** Writing – review & editing, Investigation, Formal analysis. **Xuliang Luo:** Writing – review & editing, Formal analysis. **Łukasz Kurpaska:** Writing – review & editing. **Feng Fang:** Writing – review & editing, Supervision. **Jianqing Jiang:** Writing – review & editing. **Hyoung Seop Kim:** Writing – review & editing. **Wenyi Huo:** Writing – review & editing, Writing – original draft, Supervision, Methodology, Conceptualization.

Declaration of competing interest

The authors declare that they have no known competing financial interests or personal relationships that could have appeared to influence the work reported in this paper.

Acknowledgments

The work was supported by the Natural Science Foundation of Jiangsu Province, China (BK20220428), and the National Natural Science Foundation of China (52171110). We also acknowledge support from the European Union Horizon 2020 research and innovation program under grant agreement no. 857470, the European Regional Development Fund via the Foundation for Polish Science International Research Agenda PLUS program grant no. MAB PLUS/2018/8, and the National Research Foundation of Korea (NRF) grant funded by the Korea government (MSIP) (NRF-2021R1A2C3006662, NRF-2022R1A5A1030054). The publication was created within the framework of the project of the Minister of Science and Higher Education “Support for the activities of Centres of Excellence established in Poland under Horizon 2020” under contract no. MEiN/2023/DIR/3795.

Appendix

.

Table A1

Compositions of HEOs and the parameters ΔX, VEC, ΔS_{mix}, ΔH_{mix}, δ, phase structures and synthesis methods.

High-entropy oxide systems	ΔX	VEC	ΔS_{mix} ($J\cdot K^{-1}\cdot mol^{-1}$)	ΔH_{mix} ($kJ\cdot mol^{-1}$)	δ (%)	Phases	Synthesis methods	Ref.
$(MgCoCuNiZn)O$	0.231	8.80	13.38	−1.76	9.96	Rock salt	Solid-state synthesis	[46]
$(MgCoNiZn)_{0\cdot 84}Cu_{0\cdot 16}O$	0.233	8.69	13.34	−2.28	10.09	Rock salt	Epitaxial growth	[43]
$(MgCoNiZn)_{0\cdot 82}Cu_{0\cdot 18}O$	0.232	8.75	13.37	−2.01	10.03	Rock salt	Epitaxial growth	[43]
$(MgCoNiZn)_{0\cdot 72}Cu_{0\cdot 28}O$	0.225	9.02	13.23	−0.85	9.65	Rock salt	Epitaxial growth	[43]
$(Al_{0\cdot 31}Cr_{0\cdot 20}Fe_{0\cdot 14}Ni_{0\cdot 35})O$	0.132	6.75	11.04	−16.40	6.60	Rock salt	Sputtering method	[47]
$(Mg_{0\cdot 2225}Co_{0\cdot 2225}Ni_{0\cdot 2225}Cu_{0\cdot 11}Zn_{0\cdot 2225})O$	0.236	8.55	13.14	−2.98	10.24	Rock salt	Epitaxial growth	[48]
$(Mg_{0\cdot 2075}Co_{0\cdot 2075}Ni_{0\cdot 2075}Cu_{0\cdot 17}Zn_{0\cdot 2075})O$	0.233	8.72	13.36	−2.14	10.06	Rock salt	Epitaxial growth	[48]
$(Mg_{0\cdot 19}Co_{0\cdot 19}Ni_{0\cdot 19}Cu_{0\cdot 24}Zn_{0\cdot 19})O$	0.228	8.91	13.34	−1.28	9.81	Rock salt	Epitaxial growth	[48]
$(Mg_{0\cdot 1825}Co_{0\cdot 1825}Ni_{0\cdot 1825}Cu_{0\cdot 27}Zn_{0\cdot 1825})O$	0.226	8.99	13.26	−0.95	9.69	Rock salt	Epitaxial growth	[48]
$(Mg_{0\cdot 1825}Co_{0\cdot 27}Ni_{0\cdot 1825}Cu_{0\cdot 1825}Zn_{0\cdot 1825})O$	0.225	8.82	13.26	−1.21	9.81	Rock salt	Epitaxial growth	[48]
$(Mg_{0\cdot 1675}Co_{0\cdot 33}Ni_{0\cdot 1675}Cu_{0\cdot 0\cdot 1675}Zn_{0\cdot 1675})O$	0.218	8.83	12.99	−0.80	9.65	Rock salt	Epitaxial growth	[48]
$(CoMgNiZn)O$	0.240	8.25	11.53	−4.75	10.53	Rock salt	Flame spray pyrolysis	[44]
$(CoCuMgNi)O$	0.254	8.00	11.53	1.50	11.08	Rock salt	Flame spray pyrolysis	[44]
$(CuMgNiZn)O$	0.244	8.75	11.53	−3.75	10.09	Rock salt	Flame spray pyrolysis	[44]
$(MgNiCuCoZnCr)O$	0.212	8.33	14.90	2.11	9.66	Rock salt	Solid-state synthesis	[20]
$(MgCoNiCuZn)_{0\cdot 8}(LiFe)_{0\cdot 2}O$	0.309	7.94	16.02	1.77	10.02	Rock salt	Solid-state synthesis	[49]
$(MgCoNiZn)_{0\cdot 8}(LiGa)_{0\cdot 2}O$	0.307	6.70	14.53	−5.64	9.82	Rock salt	Solid-state synthesis	[49]
$(MgCoCuZn)_{0\cdot 8}(LiGa)_{0\cdot 2}O$	0.305	6.90	14.53	−2.12	9.32	Rock salt	Solid-state synthesis	[49]
$(MgNiCuZn)_{0\cdot 8}(LiGa)_{0\cdot 2}O$	0.310	7.10	14.53	−5.08	9.41	Rock salt	Solid-state synthesis	[49]
$(MgCoNiCuZn)_{0\cdot 95}Mn_{0\cdot 05}O$	0.228	8.71	14.36	−1.78	9.71	Rock salt	Solid-state synthesis	[50]
$(Mg_{0\cdot 22}Co_{0\cdot 22}Ni_{0\cdot 23}Cu_{0\cdot 21}Zn_{0\cdot 12})O$	0.241	8.47	13.19	−0.74	10.44	Rock salt	Sol-gel methods	[51]

(*continued on next page*)

Table A1 (*continued*)

High-entropy oxide systems	ΔX	VEC	ΔS_{mix} (J·K^{-1}·mol^{-1})	ΔH_{mix} (kJ·mol^{-1})	δ (%)	Phases	Synthesis methods	Ref.
$(MgCoNiCu)_{0\cdot8}(LiGa)_{0\cdot2}O$	0.326	6.50	14.53	−1.40	10.50	Rock salt	Solid-state synthesis	[49]
$(CoNiCuZn)_{0\cdot8}(LiGa)_{0\cdot2}O$	0.273	8.50	14.53	−3.08	6.74	Rock salt	Solid-state synthesis	[49]
$(CoMgMnNiZn)(AlCoCrFeMn)_2O_4$	0.166	7.07	16.56	−6.68	7.65	Spinel	Solid-state synthesis	[52]
$(MgCoNiCuZn)Al_2O_4$	0.117	5.27	9.75	−10.99	4.98	Spinel	Solid-state synthesis	[53]
$(MgTiZnCuFe)_3O_4$	0.211	7.40	13.38	0.64	9.31	Spinel	Solid-state synthesis	[54]
$(FeCoNiCrMn)_3O_4$	0.138	8.00	13.38	−4.16	3.27	Spinel	Solid-state synthesis	[55]
$(MgFeCoNiCu)Fe_2O_4$	0.136	8.00	7.89	5.58	7.04	Spinel	Spark plasma sintering	[24]
$(MgCoNiCuZn)Fe_2O_4$	0.141	8.27	9.75	5.49	7.38	Spinel	Solid-state synthesis	[24]
$(MgMnCoNiCu)Fe_2O_4$	0.152	8.13	9.75	5.60	7.44	Spinel	Solid-state synthesis	[24]
$(MnFeCoNiCu)Fe_2O_4$	0.140	8.20	7.89	6.19	7.39	Spinel	Solid-state synthesis	[24]
$(MnFeCoNiCu)_3O_4$	0.135	9.00	13.38	1.76	3.18	Spinel	Solid-state synthesis	[24]
$(MgCoNiCuZn)Cr_2O_4$	0.137	6.93	9.75	5.14	7.18	Spinel	Solid-state synthesis	[24]
$(MgFeCoNiCu)Cr_2O_4$	0.142	6.67	9.75	4.87	6.88	Spinel	Solid-state synthesis	[24]
$(MgMnCoNiCu)Cr_2O_4$	0.141	6.60	9.75	4.92	6.97	Spinel	Solid-state synthesis	[24]
$(CrFeMgMnNi)_3O_4$	0.212	6.60	13.38	5.12	10.32	Spinel	Solid-state synthesis	[55]
$(FeCoNiCuZn)Al_2O_4$	0.119	5.33	9.75	−9.05	5.65	Spinel	Solution combustion method	[56]
$(MgFeCoNiCr)_3O_4$	0.092	8.80	13.38	3.20	1.05	Spinel	Hydrothermal method	[57]
$(MgCoNiCuZn)_{0\cdot95}Li_{0\cdot05}O$	0.278	8.41	14.36	−1.70	10.00	Spinel	Solid-state synthesis	[14]
MgCoNiCuZnLiO	0.350	7.50	14.90	−1.56	9.96	Spinel	Solid-state synthesis	[14]
$(MgCoNiCuZn)_{0\cdot98}Li_{0\cdot02}O$	0.252	8.64	13.93	−1.74	9.97	Spinel	Solid-state synthesis	[14]
$(MgCoNiCuZn)_{0\cdot96}Li_{0\cdot04}O$	0.270	8.49	14.24	−1.71	9.99	Spinel	Solid-state synthesis	[14]
$(MgCoNiCuZn)_{0\cdot94}Li_{0\cdot06}O$	0.286	8.33	14.47	−1.69	10.00	Spinel	Solid-state synthesis	[14]
$(MgCoNiCuZn)_{0\cdot92}Li_{0\cdot08}O$	0.301	8.18	14.63	−1.67	10.00	Spinel	Solid-state synthesis	[14]
$(MgCoNiCuZn)_{0\cdot90}Li_{0\cdot10}O$	0.314	8.02	14.75	−1.64	10.00	Spinel	Solid-state synthesis	[14]
$(MgCoNiCuZn)_{0\cdot80}Li_{0\cdot20}O$	0.364	7.24	14.87	−1.51	9.91	Spinel	Solid-state synthesis	[14]
$(MgCoNiCuZn)_{0\cdot70}Li_{0\cdot30}O$	0.394	6.46	14.45	−1.37	9.68	Spinel	Solid-state synthesis	[14]
$(MgCoNiCuZn)_{0\cdot90}Na_{0\cdot10}O$	0.325	8.02	14.75	6.13	14.09	Spinel	Solid-state synthesis	[14]
(NiFeCoCrAl)O	0.120	7.20	13.38	−12.32	5.76	Spinel	Sol-gel methods	[58]
$(MgCoNiCuZn)_{0\cdot95}Ti_{0\cdot05}O$	0.229	8.56	14.36	−4.29	9.82	Spinel	Solid-state synthesis	[14]
$(GdLaNdSmY)CoO_3$	0.358	6.00	12.45	−20.60	18.01	Perovskite	Nebulised spray pyrolysis	[17]
$(GdLaNdSmY)(CoCrMnFeNi)O_3$	0.317	5.50	19.14	−8.52	17.48	Perovskite	Nebulised spray pyrolysis	[59]
$(GdLaNdSmY)(CoCrFeMnNi)O_3$	0.317	5.50	19.14	−8.52	17.48	Perovskite	Nebulised spray pyrolysis	[17]
$La(CoCrFeMnNi)O_3$	0.347	5.50	12.45	−4.84	19.52	Perovskite	Nebulised spray pyrolysis	[17]
$(GdLaNdSmY)FeO_3$	0.333	5.50	12.45	0.60	18.38	Perovskite	Nebulised spray pyrolysis	[17]
$(GdLaNdSmY)NiO_3$	0.373	6.50	12.45	−30.00	18.20	Perovskite	Nebulised spray pyrolysis	[17]
$(GdLaNdSmY)MnO_3$	0.194	5.00	12.45	0.00	14.36	Perovskite	Nebulised spray pyrolysis	[17]
$(GdLaNdSmY)CrO_3$	0.249	4.50	12.45	12.60	18.08	Perovskite	Nebulised spray pyrolysis	[17]
$Y(CoCrFeMnNi)O_3$	0.290	5.50	12.45	−9.84	17.51	Perovskite	Nebulised spray pyrolysis	[17]
$Sm(CoCrFeMnNi)O_3$	0.314	5.50	12.45	−9.84	17.73	Perovskite	Nebulised spray pyrolysis	[17]
$Nd(CoCrFeMnNi)O_3$	0.328	5.50	12.45	−8.24	12.97	Perovskite	Nebulised spray pyrolysis	[17]
$GbCoCrFeMnNi)O_3$	0.299	5.50	12.45	−9.84	17.50	Perovskite	Nebulised spray pyrolysis	[17]
$(CeLaPrSm)O_2$	0.025	3.00	11.53	0.00	4.76	Fluorite	Nebulised spray pyrolysis	[16]
$(CeLaSmY)O_2$	0.047	3.00	11.53	0.00	1.67	Fluorite	Nebulised spray pyrolysis	[16]
$(CeLaNdPrSmY)O_2$	0.039	3.00	14.90	0.00	5.10	Fluorite	Nebulised spray pyrolysis	[16]
$(CeGdLaNdPSmY)O_2$	0.041	3.00	16.18	0.00	4.75	Fluorite	Nebulised spray pyrolysis	[16]
$(HfZrCeY)O_{2\text{-}\delta}$	0.081	2.50	11.53	11.50	6.63	Fluorite	Spark plasma sintering	[22]
$(HfZrCe)_{0.75}(YYb)_{0.25}O_{2\text{-}\delta}$	0.094	2.50	12.97	19.88	6.28	Fluorite	Spark plasma sintering	[22]
$(HfZrCe)_{0.75}(YCa)_{0.25}O_{2\text{-}\delta}$	0.115	2.38	12.97	20.31	8.30	Fluorite	Spark plasma sintering	[22]
$(HfZrCe)_{0.75}(Y_{0\cdot125}Gd_{0\cdot125})_{0.25}O_{2\text{-}\delta}$	0.082	2.50	12.97	11.50	6.63	Fluorite	Spark plasma sintering	[22]
$(HfZrCe)_{0.6}(Y_{0\cdot2}Gd_{0\cdot2})_{0.4}O_{2\text{-}\delta}$	0.075	2.60	13.38	10.56	6.32	Fluorite	Spark plasma sintering	[22]
$(GdLaCeHfZr)O_2$	0.093	2.60	13.38	11.84	7.12	Fluorite	Chemical co-precipitation	[60]
$(GdLaYHfZr)O_2$	0.081	2.60	13.38	10.88	6.95	Fluorite	Chemical co-precipitation	[60]
$(HfZrCe)_{0.6}(YYb)_{0.4}O_{2\text{-}\delta}$	0.092	2.60	13.38	22.08	5.92	Fluorite	Spark plasma sintering	[22]
$(HfZrCe)_{0.75}(YbGd)_{0.25}O_{2\text{-}\delta}$	0.095	2.50	12.97	19.88	6.28	Fluorite	Spark plasma sintering	[22]
$(HfZrCe)_{0.6}(YbGd)_{0.4}O_{2\text{-}\delta}$	0.093	2.60	13.38	22.08	5.92	Fluorite	Spark plasma sintering	[22]
$(CeLaPrSmY)O_{2\text{-}\delta}$	0.043	3.00	13.38	0.00	4.25	Fluorite	Nebulised spray pyrolysis	[61]

Data availability

Data will be made available on request.

References

[1] Y. Chen, Z. Lai, X. Zhang, Z. Fan, Q. He, C. Tan, H. Zhang, Phase engineering of nanomaterials, Nat. Rev. Chem. 4 (5) (2020) 243–256.

[2] Q. Yun, Y. Ge, Z. Shi, J. Liu, X. Wang, A. Zhang, B. Huang, Y. Yao, Q. Luo, L. Zhai, J. Ge, Y. Peng, C. Gong, M. Zhao, Y. Qin, C. Ma, G. Wang, Q. Wa, X. Zhou, Z. Li, S. Li, W. Zhai, H. Yang, Y. Ren, Y. Wang, L. Li, X. Ruan, Y. Wu, B. Chen, Q. Lu, Z. Lai, Q. He, X. Huang, Y. Chen, H. Zhang, Recent progress on phase engineering of nanomaterials, Chem. Rev. 123 (23) (2023) 13489–13692.

[3] X. Feng, B. Zhai, R. Cheng, L. Yin, Y. Wen, J. Jiang, H. Wang, Z. Li, Y. Zhu, J. He, Phase engineering of 2D spinel-type manganese oxides, Adv. Mater. 35 (42) (2023) 2304118.

[4] H. Li, X. Zhou, W. Zhai, S. Lu, J. Liang, Z. He, H. Long, T. Xiong, H. Sun, Q. He, Z. Fan, H. Zhang, Phase engineering of nanomaterials for clean energy and catalytic applications, Adv. Energy Mater. 10 (40) (2020) 2002019.

[5] B. Cantor, I.T.H. Chang, P. Knight, A.J.B. Vincent, Microstructural development in equiatomic multicomponent alloys, Mater. Sci. Eng. A 375–377 (2004) 213–218.

[6] J.W. Yeh, S.K. Chen, S.J. Lin, J.Y. Gan, T.S. Chin, T.T. Shun, C.H. Tsau, S. Y. Chang, Nanostructured high-entropy alloys with multiple principal elements: novel alloy design concepts and outcomes, Adv. Eng. Mater. 6 (5) (2004) 299–303.

[7] M.H. Tsai, J.W. Yeh, High-entropy alloys: A critical review, Mater. Res. Lett. 2 (3) (2014) 107–123.

[8] J.W. Yeh, Recent progress in high-entropy alloys, Ann. Chim. Sci. Mat 31 (2006) 633–648.

[9] C.M. Rost, E. Sachet, T. Borman, A. Moballegh, E.C. Dickey, D. Hou, J.L. Jones, S. Curtarolo, J.-P. Maria, Entropy-stabilized oxides, Nat. Commun. 6 (1) (2015) 8485.

[10] S. Wang, H. Yan, W. Huo, A. Davydok, M. Zając, J. Stępień, H. Feng, Z. Xie, J. K. Shang, P.H.C. Camargo, J. Jiang, F. Fang, Engineering multiple nano-twinned high entropy alloy electrocatalysts toward efficient water electrolysis, Appl. Catal. B 363 (2025) 124791.

[11] T. Jin, X. Sang, R.R. Unocic, R.T. Kinch, X. Liu, J. Hu, H. Liu, S. Dai, Mechanochemical-assisted synthesis of high-entropy metal nitride via a soft urea strategy, Adv. Mater. 30 (23) (2018) 1707512.

[12] R. He, S. Wang, L. Yang, S. Horta, Y. Ding, C. Di, X. Zhang, Y. Xu, M. Ibáñez, Y. Zhou, S. Mebs, H. Dau, J.N. Hausmann, W. Huo, P.W. Menezes, A. Cabot, Active site switching on high entropy phosphides as bifunctional oxygen electrocatalysts for rechargeable/robust Zn-Air battery, Energ. Environ. Sci. 17 (2024) 7193–7208.

[13] A. Sarkar, R. Djenadic, N.J. Usharani, K.P. Sanghvi, V.S.K. Chakravadhanula, A. S. Gandhi, H. Hahn, S.S. Bhattacharya, Nanocrystalline multicomponent entropy stabilised transition metal oxides, J. Eur. Ceram. Soc. 37 (2) (2017) 747–754.

[14] D. Bérardan, S. Franger, A.K. Meena, N. Dragoe, Room temperature lithium superionic conductivity in high entropy oxides, J. Mater. Chem. A 4 (24) (2016) 9536–9541.

[15] A. Sarkar, C. Loho, L. Velasco, T. Thomas, S.S. Bhattacharya, H. Hahn, R. Djenadic, Multicomponent equiatomic rare earth oxides with a narrow band gap and associated praseodymium multivalency, Dalton Trans. 46 (36) (2017) 12167–12176.

[16] R. Djenadic, A. Sarkar, O. Clemens, C. Loho, M. Botros, V.S.K. Chakravadhanula, C. Kübel, S.S. Bhattacharya, A.S. Gandhi, H. Hahn, Multicomponent equiatomic rare earth oxides, Mater. Res. Lett. 5 (2) (2017) 102–109.

[17] A. Sarkar, R. Djenadic, D. Wang, C. Hein, R. Kautenburger, O. Clemens, H. Hahn, Rare earth and transition metal based entropy stabilised perovskite type oxides, J. Eur. Ceram. Soc. 38 (5) (2018) 2318–2327.

[18] A. Sarkar, Q. Wang, A. Schiele, M.R. Chellali, S.S. Bhattacharya, D. Wang, T. Brezesinski, H. Hahn, L. Velasco, B. Breitung, High-entropy oxides: fundamental aspects and electrochemical properties, Adv. Mater. 31 (26) (2019) 1806236.

[19] G.M. Tomboc, X. Zhang, S. Choi, D. Kim, L.Y.S. Lee, K. Lee, Stabilization, characterization, and electrochemical applications of high-entropy oxides: critical assessment of crystal phase-properties relationship, Adv. Funct. Mater. 32 (43) (2022) 2205142.

[20] J.L. Braun, C.M. Rost, M. Lim, A. Giri, D.H. Olson, G.N. Kotsonis, G. Stan, D. W. Brenner, J.-P. Maria, P.E. Hopkins, Charge-induced disorder controls the thermal conductivity of entropy-stabilized oxides, Adv. Mater. 30 (51) (2018) 1805004.

[21] Y. Pu, D. Moseley, Z. He, K.C. Pitike, M.E. Manley, J. Yan, V.R. Cooper, V. Mitchell, V.K. Peterson, B. Johannessen, R.P. Hermann, P. Cao, (Mg,Mn,Fe,Co,Ni)O: A rocksalt high-entropy oxide containing divalent Mn and Fe, Sci. Adv. 9 (38) (2023) eadi8809.

[22] J. Gild, M. Samiee, J.L. Braun, T. Harrington, H. Vega, P.E. Hopkins, K. Vecchio, J. Luo, High-entropy fluorite oxides, J. Eur. Ceram. Soc. 38 (10) (2018) 3578–3584.

[23] S.L. Liew, X.P. Ni, F. Wei, S.Y. Tan, M.T. Luai, P.C. Lim, S.L. Teo, N.B.M. Rafiq, J. Zhou, S. Wang, High-entropy fluorite oxides: Atomic stabiliser effects on thermal-mechanical properties, J. Eur. Ceram. Soc. 42 (14) (2022) 6608–6613.

[24] B. Musicó, Q. Wright, T.Z. Ward, A. Grutter, E. Arenholz, D. Gilbert, D. Mandrus, V. Keppens, Tunable magnetic ordering through cation selection in entropic spinel oxides, Phys. Rev. Mater. 3 (10) (2019) 104416.

[25] Z. Sun, Y. Zhao, C. Sun, Q. Ni, C. Wang, H. Jin, High entropy spinel-structure oxide for electrochemical application, Chem. Eng. J. 431 (2022) 133448.

[26] A. Mao, F. Quan, H.Z. Xiang, Z.G. Zhang, K. Kuramoto, A.L. Xia, Facile synthesis and ferrimagnetic property of spinel $(CoCrFeMnNi)_3O_4$ high-entropy oxide nanocrystalline powder, J. Mol. Struct. 1194 (2019) 11–18.

[27] T.X. Nguyen, Y.C. Liao, C.C. Lin, Y.H. Su, J.M. Ting, Advanced high entropy perovskite oxide electrocatalyst for oxygen evolution reaction, Adv. Funct. Mater. 31 (27) (2021) 2101632.

[28] R. Witte, A. Sarkar, R. Kruk, B. Eggert, R.A. Brand, H. Wende, H. Hahn, High-entropy oxides: An emerging prospect for magnetic rare-earth transition metal perovskites, Phys. Rev. Mater. 3 (3) (2019) 034406.

[29] Y. Zhang, Y.J. Zhou, J.P. Lin, G.L. Chen, P.K. Liaw, Solid-solution phase formation rules for multi-component alloys, Adv. Eng. Mater. 10 (6) (2008) 534–538.

[30] X. Yang, Y. Zhang, Prediction of high-entropy stabilized solid-solution in multi-component alloys, Mater. Chem. Phys. 132 (2) (2012) 233–238.

[31] S. Guo, C. Ng, J. Lu, C.T. Liu, Effect of valence electron concentration on stability of fcc or bcc phase in high entropy alloys, J. Appl. Phys. 109 (10) (2011) 103505.

[32] Y. Dong, Y. Lu, L. Jiang, T. Wang, T. Li, Effects of electro-negativity on the stability of topologically close-packed phase in high entropy alloys, Intermetallics 52 (2014) 105–109.

[33] Y. Li, Ł. Kurpaska, E. Lu, Z. Xie, H.S. Kim, W. Huo, Body-centered cubic phase stability in cobalt-free refractory high-entropy alloys, Results Phys. 60 (2024) 107688.

[34] Y. Li, A. Olejarz, Ł. Kurpaska, E. Lu, M.J. Alava, H.S. Kim, W. Huo, Designing cobalt-free face-centered cubic high-entropy alloys: A strategy using d-orbital energy level, Int. J. Refract. Met. Hard Mater. 124 (2024) 106834.

[35] V.M. Goldschmidt, Die gesetze der krystallochemie, Naturwiss. 14 (21) (1926) 477–485.

[36] T. Rom, A.K.P. Poojita, Structure-property relationship of double perovskite oxide towards trifunctional electrocatalytic activity: Strategy for designing and development, Chem. Cat. Chem. 15 (20) (2023) e20230774.

[37] L. Spiridigliozzi, C. Ferone, R. Cioffi, G. Dell'Agli, A simple and effective predictor to design novel fluorite-structured High Entropy Oxides (HEOs), Acta Mater. 202 (2021) 181–189.

[38] M. Brahlek, M. Gazda, V. Keppens, A.R. Mazza, S.J. McCormack, A. Mielewczyk-Gryń, B. Musico, K. Page, C.M. Rost, S.B. Sinnott, C. Toher, T.Z. Ward, A. Yamamoto, What is in a name: Defining "high entropy" oxides, APL Mater. 10 (11) (2022) 110902.

[39] D.B. Miracle, O.N. Senkov, A critical review of high entropy alloys and related concepts, Acta Mater. 122 (2017) 448–511.

[40] S. Jiang, T. Hu, J. Gild, N. Zhou, J. Nie, M. Qin, T. Harrington, K. Vecchio, J. Luo, A new class of high-entropy perovskite oxides, Scr. Mater. 142 (2018) 116–120.

[41] M. Zhang, X. Shi, Z. Li, H. Xu, G. Li, Corrosion behaviors and mechanism of $CrFeNi_2$ based high-entropy alloys, Corros. Sci. 207 (2022) 110562.

[42] T. Borkar, V. Chaudhary, B. Gwalani, D. Choudhuri, C.V. Mikler, V. Soni, T. Alam, R.V. Ramanujan, R. Banerjee, A combinatorial approach for assessing the magnetic properties of high entropy alloys: Role of Cr in $AlCo_xCr_{1-x}FeNi$, Adv. Eng. Mater. 19 (8) (2017) 1700048.

[43] D. Berardan, A.K. Meena, S. Franger, C. Herrero, N. Dragoe, Controlled Jahn-Teller distortion in (MgCoNiCuZn)O-based high entropy oxides, J. Alloys Compd. 704 (2017) 693–700.

[44] N.J. Usharani, P. Arivazhagan, T. Thomas, S.S. Bhattacharya, Factors determining the band gap of a nanocrystalline multicomponent equimolar transition metal based high entropy oxide (Co,Cu,Mg,Ni,Zn)O, Mater. Sci. Eng. B 283 (2022) 115847.

[45] Y. Jiao, J. Dai, Z. Fan, J. Cheng, G. Zheng, L. Grema, J. Zhong, H.-F. Li, D. Wang, Overview of high-entropy oxide ceramics, Mater. Today 77 (2024) 92–117.

[46] A.D. Dupuy, X. Wang, J.M. Schoenung, Entropic phase transformation in nanocrystalline high entropy oxides, Mater. Res. Lett. 7 (2) (2019) 60–67.

[47] Z.M. Yang, K. Zhang, N. Qiu, H.B. Zhang, Y. Wang, J. Chen, Effects of helium implantation on mechanical properties of $(Al_{0.31}Cr_{0.20}Fe_{0.14}Ni_{0.35})O$ high entropy oxide films, Chin. Phys. B 28 (4) (2019) 046201.

[48] P.B. Meisenheimer, L.D. Williams, S.H. Sung, J. Gim, P. Shafer, G.N. Kotsonis, J. P. Maria, M. Trassin, R. Hovden, E. Kioupakis, J.T. Heron, Magnetic frustration control through tunable stereochemically driven disorder in entropy-stabilized oxides, Phys. Rev. Mater. 3 (10) (2019) 104420.

[49] M.P. Jimenez-Segura, T. Takayama, D. Bérardan, A. Hoser, M. Reehuis, H. Takagi, N. Dragoe, Long-range magnetic ordering in rocksalt-type high-entropy oxides, J. Appl. Phys. 114 (12) (2019) 122401.

[50] J. Chen, W. Liu, J. Liu, X. Zhang, M. Yuan, Y. Zhao, J. Yan, M. Hou, J. Yan, M. Kunz, N. Tamura, H. Zhang, Z. Yin, Stability and compressibility of cation-doped high-entropy oxide $MgCoNiCuZnO_5$, J. Phys. Chem. C 123 (29) (2019) 17735–17744.

[51] G.R. Rao, M.M. Ali, S. Roychowdhury, L. Prasad, Promising oxygen storage capacity of equimolar high entropy transition metal oxide (MgCoNiCuZn)O, Mater. Lett. 304 (2021) 130635.

[52] M. Fracchia, M. Manzoli, U. Anselmi-Tamburini, P. Ghigna, A new eight-cation inverse high entropy spinel with large configurational entropy in both tetrahedral and octahedral sites: Synthesis and cation distribution by X-ray absorption spectroscopy, Scr. Mater. 188 (2020) 26–31.

[53] S. Marik, D. Singh, B. Gonano, F. Veillon, D. Pelloquin, Y. Bréard, Enhanced magnetic frustration in a new high entropy diamond lattice spinel oxide, Scr. Mater. 186 (2020) 366–369.

[54] H. Chen, N. Qiu, B. Wu, Z. Yang, S. Sun, Y. Wang, A new spinel high-entropy oxide $(Mg_{0.2}Ti_{0.2}Zn_{0.2}Cu_{0.2}Fe_{0.2})_3O_4$ with fast reaction kinetics and excellent stability as an anode material for lithium ion batteries, RSC Adv. 10 (16) (2020) 9736–9744.

[55] M. Stygar, J. Dąbrowa, M. Moździerz, M. Zajusz, W. Skubida, K. Mroczka, K. Berent, K. Świerczek, M. Danielewski, Formation and properties of high entropy oxides in Co-Cr-Fe-Mg-Mn-Ni-O system: Novel $(Cr,Fe,Mg,Mn,Ni)_3O_4$ and $(Co,Cr,Fe,Mg,Mn)_3O_4$ high entropy spinels, J. Eur. Ceram. Soc. 40 (4) (2020) 1644–1650.

[56] R.R. Katzbaer, F.M. dos Santos Vieira, I. Dabo, Z. Mao, R.E. Schaak, Band gap narrowing in a high-entropy spinel oxide semiconductor for enhanced oxygen evolution catalysis, J. Am. Chem. Soc. 145 (12) (2023) 6753–6761.

[57] Y. Guo, X. Zhang, H. Wei, H.-T. Yu, Y. Xie, Construction of spinel $(Fe_{0.2}Co_{0.2}Ni_{0.2}Cr_{0.2}M_{0.2})_3O_4$ (M = Mg, Mn, Zn, and Cu) high-entropy oxides with tunable valance states for oxygen evolution reaction, J. Alloys Compd. 989 (2024) 174304.

[58] M.S. Lal, R. Sundara, High entropy oxides-A cost-effective catalyst for the growth of high yield carbon nanotubes and their energy applications, ACS Appl. Mater. Interfaces 11 (34) (2019) 30846–30857.

[59] M.R. Chellali, A. Sarkar, S.H. Nandam, S.S. Bhattacharya, B. Breitung, H. Hahn, L. Velasco, On the homogeneity of high entropy oxides: An investigation at the atomic scale, Scr. Mater. 166 (2019) 58–63.

[60] M. Anandkumar, S. Bhattacharya, A.S. Deshpande, Low temperature synthesis and characterization of single phase multi-component fluorite oxide nanoparticle sols, RSC Adv. 9 (46) (2019) 26825–26830.

[61] B. Cheng, H. Lou, A. Sarkar, Z. Zeng, F. Zhang, X. Chen, L. Tan, V. Prakapenka, E. Greenberg, J. Wen, R. Djenadic, H. Hahn, Q. Zeng, Pressure-induced tuning of lattice distortion in a high-entropy oxide, Commun. Chem. 2 (1) (2019) 114.

[62] L. Spiridigliozzi, C. Ferone, R. Cioffi, G. Accardo, D. Frattini, G. Dell'Agli, Entropy-stabilized oxides owning fluorite structure obtained by hydrothermal treatment, Materials 13 (3) (2020) 558.

[63] B.L. Musicó, D. Gilbert, T.Z. Ward, K. Page, E. George, J. Yan, D. Mandrus, V. Keppens, The emergent field of high entropy oxides: Design, prospects,

challenges, and opportunities for tailoring material properties, APL Mater. 8 (4) (2020) 040912.

[64] C.S. Wu, P.H. Tsai, C.M. Kuo, C.W. Tsai, Effect of atomic size difference on the microstructure and mechanical properties of high-entropy alloys, Entropy 20 (12) (2018) 967.

[65] J. Gild, Y. Zhang, T. Harrington, S. Jiang, T. Hu, M.C. Quinn, W.M. Mellor, N. Zhou, K. Vecchio, J. Luo, High-entropy metal diborides: A new class of high-entropy materials and a new type of ultrahigh temperature ceramics, Sci. Rep. 6 (1) (2016) 37946.

[66] K. Fang, Y. Zhang, J. Yin, T. Yang, K. Li, L. Wei, J. Li, W. He, Hydrogel beads based on carboxymethyl cassava starch/alginate enriched with MgFe$_2$O$_4$ nanoparticles for controlling drug release, Int. J. Biol. Macromol. 220 (2022) 573–588.

[67] M. Mureddu, F. Ferrara, A. Pettinau, Highly efficient CuO/ZnO/ZrO$_2$@SBA-15 nanocatalysts for methanol synthesis from the catalytic hydrogenation of CO$_2$, Appl. Catal. B 258 (2019) 117941.

[68] A. Takeuchi, A. Inoue, Classification of bulk metallic glasses by atomic size difference, heat of mixing and period of constituent elements and its application to characterization of the main alloying element, Mater. Trans. 46 (12) (2005) 2817–2829.

[69] Y. Zuo, T. Meng, H. Tian, L. Ling, H. Zhang, H. Zhang, X. Sun, S. Cai, Enhanced H$^+$ storage of a MnO$_2$ cathode via a mno$_2$ nanolayer interphase transformed from manganese phosphate, ACS Nano 17 (6) (2023) 5600–5608.

[70] J. Dąbrowa, M. Stygar, A. Mikuła, A. Knapik, K. Mroczka, W. Tejchman, M. Danielewski, M. Martin, Synthesis and microstructure of the (Co,Cr,Fe,Mn,Ni)$_3$O$_4$ high entropy oxide characterized by spinel structure, Mater. Lett. 216 (2018) 32–36.

[71] Y. Yao, S. Wang, C. Wang, Z. Wu, C. Xiao, X. Guo, X. Yan, J. Qi, Y. Zhou, Z. Zhu, Y. Yang, X. Li, J. Li, Prussian blue analogue-derived high-entropy alloy nanoarchitectonics for efficient Fenton-like catalysis, J. Mater. Chem. A 12 (17) (2024) 10081–10089.

[72] C. Wei, C. Li, D. Qu, B. Liao, D. Han, Z.-H. Sun, L. Niu, High-entropy selenides derived from prussian blue analogues as electrode materials for sodium-ion batteries, J. Colloid Interface Sci. 675 (2024) 139–149.

[73] M. Du, P. Geng, C. Pei, X. Jiang, Y. Shan, W. Hu, L. Ni, H. Pang, High-entropy prussian blue analogues and their oxide family as sulfur hosts for lithium-sulfur batteries, Angew. Chem., Int. Ed. 61 (41) (2022) e202209350.

[74] S. Ye, J. Zhu, S. Zhu, Y. Zhao, M. Li, Z. Huang, H. Wang, J. He, Design strategies for perovskite-type high-entropy oxides with applications in optics, ACS Appl. Mater. Interfaces 15 (40) (2023) 47475–47486.

[75] Z.Y. Liu, Y. Liu, Y. Xu, H. Zhang, Z. Shao, Z. Wang, H. Chen, Novel high-entropy oxides for energy storage and conversion: From fundamentals to practical applications, Green Energy Environ. 8 (5) (2023) 1341–1357.

[76] M. Anandkumar, E. Trofimov, Synthesis, properties, and applications of high-entropy oxide ceramics: Current progress and future perspectives, J. Alloys Compd. 960 (2023) 170690.

[77] K. Du, Y. Liu, Y. Yang, F. Cui, J. Wang, M. Han, J. Su, J. Wang, X. Han, Y. Hu, High entropy oxides modulate atomic-level interactions for high-performance aqueous zinc-ion batteries, Adv. Mater. 35 (51) (2023) 2301538.

[78] S.A. Khan, M.A. Rahman, M. Khraisheh, I.G. Hassan, Advances in 3D printed periodic lattice structures for energy research: Energy storage, transport and conversion applications, Mater. Des. 239 (2024) 112773.

[79] H. Chen, J. Fu, P. Zhang, H. Peng, C.W. Abney, K. Jie, X. Liu, M. Chi, S. Dai, Entropy-stabilized metal oxide solid solutions as CO oxidation catalysts with high-temperature stability, J. Mater. Chem. A 6 (24) (2018) 11129–11133.

[80] Y. Pan, J.X. Liu, T.Z. Tu, W. Wang, G.J. Zhang, High-entropy oxides for catalysis: A diamond in the rough, Chem. Eng. J. 451 (2023) 138659.

[81] S. Das, S. Kumar, S. Sarkar, D. Pradhan, C.S. Tiwary, S. Chowdhury, High entropy spinel oxide nanoparticles for visible light-assisted photocatalytic degradation of binary mixture of antibiotic pollutants in different water matrixes, J. Mater. Chem. A 12 (27) (2024) 16815–16830.

[82] M. Anandkumar, P.K. Kannan, S. Sudarsan, E.A. Trofimov, High-entropy oxide (CeGdHfPrZr)O$_2$ nanoparticles as reusable photocatalyst for wastewater remediation, Surf. Interfaces 51 (2024) 104815.

[83] B. Han, Q. Pan, Y. Chen, D. Liu, C. Zhou, K. Xia, Q. Gao, High-entropy perovskite oxide washcoated porous alumina ceramic as a superb catalyst for activating peroxymonosulfate to eliminate refractory organic pollutants, Chem. Eng. J. 455 (2023) 140828.

[84] T. Egami, Y. Waseda, Atomic size effect on the formability of metallic glasses, J. Non-Cryst. Solids 64 (1) (1984) 113–134.

[85] S. Guo, C.T. Liu, Phase stability in high entropy alloys: Formation of solid-solution phase or amorphous phase, Prog. Nat. Sci.: Mater. Int. 21 (6) (2011) 433–446.

[86] H. Yang, G. Lin, H. Bu, H. Liu, L. Yang, W. Wang, X. Lin, C. Fu, Y. Wang, C. Zeng, Single-phase forming ability of high-entropy ceramics from a size disorder perspective: A case study of (La$_{0.2}$Eu$_{0.2}$Gd$_{0.2}$Y$_{0.2}$Yb$_{0.2}$)$_2$Zr$_2$O$_7$, Ceram. Int. 48 (5) (2022) 6956–6965.

[87] P. Hutterer, M. Lepple, Influence of composition on structural evolution of high-entropy zirconates-cationic radius ratio and atomic size difference, J. Am. Ceram. Soc. 106 (2) (2023) 1547–1560.

[88] L. Zhang, H. Li, Z. Xiao, Criteria of predicting phase formation for MSi$_2$-type high-entropy refractory metal silicides, Mater. Des. 231 (2023) 112060.

[89] J.M. Schneider, How high is the entropy in high entropy ceramics? J. Appl. Phys. 130 (15) (2021) 150903.

[90] J. Liu, A. Wang, P. Gao, R. Bai, J. Liu, B. Du, C. Fang, Machine learning-based crystal structure prediction for high-entropy oxide ceramics, J. Am. Ceram. Soc. 107 (2) (2024) 1361–1371.

[91] R. Mitra, A. Bajpai, K. Biswas, Machine learning based approach for phase prediction in high entropy borides, Ceram. Int. 48 (12) (2022) 16695–16706.

[92] R. Mitra, A. Bajpai, K. Biswas, ADASYN-assisted machine learning for phase prediction of high entropy carbides, Comput. Mater. Sci. 223 (2023) 112142.

[93] S.J. McCormack, A. Navrotsky, Thermodynamics of high entropy oxides, Acta Mater. 202 (2021) 1–21.

[94] O.F. Dippo, N. Mesgarzadeh, T.J. Harrington, G.D. Schrader, K.S. Vecchio, Bulk high-entropy nitrides and carbonitrides, Sci. Rep. 10 (1) (2020) 21288.

[95] K. Balasubramanian, S.V. Khare, D. Gall, Valence electron concentration as an indicator for mechanical properties in rocksalt structure nitrides, carbides and carbonitrides, Acta Mater. 152 (2018) 175–185.

[96] D.G. Sangiovanni, W. Mellor, T. Harrington, K. Kaufmann, K. Vecchio, Enhancing plasticity in high-entropy refractory ceramics via tailoring valence electron concentration, Mater. Des. 209 (2021) 109932.

[97] W.M. Mellor, K. Kaufmann, O.F. Dippo, S.D. Figueroa, G.D. Schrader, K. S. Vecchio, Development of ultrahigh-entropy ceramics with tailored oxidation behavior, J. Eur. Ceram. Soc. 41 (12) (2021) 5791–5800.

[98] L. Velasco, J.S. Castillo, M.V. Kante, J.J. Olaya, P. Friederich, H. Hahn, Phase-property diagrams for multicomponent oxide systems toward materials libraries, Adv. Mater. 33 (43) (2021) 2102301.

[99] V. Strotkötter, O.A. Krysiak, J. Zhang, X. Wang, E. Suhr, W. Schuhmann, A. Ludwig, Discovery of high-entropy oxide electrocatalysts: From thin-film material libraries to particles, Chem. Mater. 34 (23) (2022) 10291–10303.

[100] Y. Wang, J. Zhu, M. Li, G. Shao, H. Wang, R. Zhang, Thermal properties of high-entropy re-disilicates controlled by high throughput composition design and optimization, Mater. Des. 236 (2023) 112485.

[101] D. de Araujo Santana, B. Ellyson, A. Clarke, K. Clarke, N. Schell, M. Kaufman, C. S. Kiminami, F.G. Coury, High-throughput strategy to design high entropy alloys with an fcc matrix, L1$_2$ precipitates, and optimized yield stress, Mater. Des. 244 (2024) 113173.

[102] H. Meng, R. Yu, Z. Tang, Z. Wen, H. Yu, Y. Chu, Formation ability descriptors for high-entropy diborides established through high-throughput experiments and machine learning, Acta Mater. 256 (2023) 119132.

[103] C. Lee, D. Xie, B.K. Derby, J.K. Baldwin, C. Tandoc, O.E. Atwani, Y.J. Hu, J. A. Valdez, N. Li, S.J. Fensin, An experimentally driven high-throughput approach to design refractory high-entropy alloys, Mater. Des. 223 (2022) 111259.

[104] M. Kumbhakar, A. Khandelwal, S.K. Jha, M.V. Kante, P. Keßler, U. Lemmer, H. Hahn, J. Aghassi-Hagmann, A. Colsmann, B. Breitung, L. Velasco, S. Schweidler, High-throughput screening of high-entropy fluorite-type oxides as potential candidates for photovoltaic applications, Adv. Energy Mater. 13 (24) (2023) 2204337.